

Fully coupled photochemistry of the deuterated ionosphere of Mars and its effects on escape of H and D

Eryn Cangi¹, Michael Chaffin¹, Roger Yelle², Bethan Gregory¹, Justin Deighan¹

¹Laboratory for Atmospheric and Space Physics, University of Colorado Boulder
²Lunar and Planetary Laboratory, University of Arizona

Key Points:

- We present the first photochemical modeling study of the deuterated ionosphere of Mars.
- Non-thermal escape dominates D loss under all solar conditions, and the processes producing hot D are similar to those producing hot H.
- The combined D/H fractionation factor is $f = 0.04\text{--}0.07$, indicating 147–158 m GEL of water loss, still less than geological estimates.

arXiv:2306.16396v1 [astro-ph.EP] 28 Jun 2023

Corresponding author: Eryn Cangi, eryn.cangi@colorado.edu

Abstract

Although deuterium (D) on Mars has received substantial attention, the deuterated ionosphere remains relatively unstudied. This means that we also know very little about non-thermal D escape from Mars, since it is primarily driven by excess energy imparted to atoms produced in ion-neutral reactions. Most D escape from Mars is expected to be non-thermal, highlighting a gap in our understanding of water loss from Mars. In this work, we set out to fill this knowledge gap. To accomplish our goals, we use an upgraded 1D photochemical model that fully couples ions and neutrals and does not assume photochemical equilibrium. To our knowledge, such a model has not been applied to Mars previously. We model the atmosphere during solar minimum, mean, and maximum, and find that the deuterated ionosphere behaves similarly to the H-bearing ionosphere, but that non-thermal escape on the order of $8000\text{--}9000\text{ cm}^{-2}\text{s}^{-1}$ dominates atomic D loss under all solar conditions. The total fractionation factor, f , is $f = 0.04\text{--}0.07$, and integrated water loss is 147–158 m GEL. This is still less than geomorphological estimates. Deuterated ions at Mars are likely difficult to measure with current techniques due to low densities and mass degeneracies with more abundant H ions. Future missions wishing to measure the deuterated ionosphere in situ will need to develop innovative techniques to do so.

Plain Language Summary

Our knowledge of ions in the martian atmosphere that contain deuterium (D), an isotope of hydrogen (H), is limited, lacking measurements and dedicated computer models. This is a problem because the expectation is that most D that escapes to space does so by gaining extra energy from ion reactions. H and D mostly exist in water on Mars, so identifying how much H and D have escaped this way is important to understanding how Mars lost all the water that it once had, transforming it from a planet that could have supported life into the hostile environment it is today. Here, we present the first one dimensional model of the Mars atmosphere that includes D-bearing ions. We report the amounts and types of H and D escape and confirm that most D gets its escape energy from ion chemistry. We also identify the specific chemical reactions that are most important, and show how many D-bearing ions we expect to find in the atmosphere that might be detectable by future missions. Finally, we calculate that a layer of water 147–158 m deep has been lost from Mars. This is still less than the amount calculated by geological studies.

1 Introduction

Mars is a natural laboratory to study how atmospheric escape shapes planetary habitability. It is now well established that a significant amount of the Mars atmosphere has been lost to space (e.g. Jakosky et al., 2018). This escape is fractionating—the relative escape efficiency is different for members of an isotope pair, such as deuterium (D) and hydrogen (H). Because on Mars, D and H are found primarily in water, D/H fractionation indicates a history of water loss (Owen et al., 1988). Understanding escape fractionation therefore contributes to understanding the long-term loss of the atmosphere and desiccation of the planet.

Geological studies indicate that Mars has likely lost 500+ meters global equivalent layer (GEL) of water (Lasue et al., 2013, and references therein), but atmospheric modeling studies typically do not find the same result, instead arriving at a smaller number of 100–250 m GEL (Cangi et al., 2020; Alsaeed & Jakosky, 2019; V. A. Krasnopolsky, 2002; V. Krasnopolsky, 2000). A key step in retrieving water loss estimates from atmospheric models is to quantify both thermal and non-thermal escape.

Thermal escape includes hydrodynamic escape, which may have occurred on early Mars and is not expected to significantly fractionate H and D (Hunten et al., 1987), but does

fractionate more massive molecules (Cassata et al., 2022; Yoshida & Kuramoto, 2020; Zahnle et al., 1990); and Jeans escape, in which a small fraction of particles escape because they have a thermal velocity in the high-energy tail of the Maxwellian velocity distribution, above planetary escape velocity. Non-thermal escape comprises all other processes that grant extra kinetic energy to atmospheric particles, then variously dubbed “suprathermal” or “hot”; most of these processes involve ion chemistry or interaction with ions and include sputtering, interactions of the planetary ionosphere with the solar wind, and ion outflow. (Impact-driven escape also falls under the non-thermal category, but doesn’t specifically involve ions, and is not expected to be fractionating.) H escape has been well-studied at Mars with atmospheric models, observations from missions, and mixes of the two (Gu et al., 2022; Chaffin et al., 2021; Chaufray, Gonzalez-Galindo, et al., 2021; Holmes et al., 2021; Stone et al., 2020; AlMaazmi et al., 2019; V. A. Krasnopolsky, 2019; Mayyasi et al., 2018; Rahmati et al., 2018; Halekas, 2017; Bhattacharyya et al., 2017; Zahnle et al., n.d.; V. A. Krasnopolsky, 2002, and others). Thermal escape of D has also been modeled (Cangi et al., 2020; Kass & Yung, 1999; Yung et al., 1988), but non-thermal escape of D sourced from planetary ion-neutral reactions has not been modeled, despite indications that non-thermal escape is the dominant loss process of D (Gacesa et al., 2012; V. A. Krasnopolsky, 2010, 2002). V. A. Krasnopolsky (2010, 2002) and V. A. Krasnopolsky et al. (1998) calculated non-thermal D escape velocities for a few select processes (solar wind charge exchange, electron impact ionization, and photoionization), but their model did not include a deuterated ionosphere, and so missed a portion of the production of hot atoms.

Cangi et al. (2020) used a 1D photochemical model of Mars’ neutral atmosphere to calculate the D/H fractionation factor f as a function of atmospheric temperatures. The model only calculated thermal escape directly; non-thermal escape was approximated by scaling the non-thermal effusion velocities given by V. A. Krasnopolsky (2002) and multiplying them by the densities of H and D at the exobase. This estimation indicated that f is several orders of magnitude larger when non-thermal escape processes are considered, motivating a more complete calculation of non-thermal escape of H and D. Here, we present this more complete treatment. The key questions about the deuterated martian ionosphere that we address are as follows.

1. What are the atmospheric densities of deuterated ions?
2. What are the dominant production mechanisms of hot H and hot D, and are they analogous or dissimilar?
3. What is the magnitude of non-thermal escape of D, and is it the dominant type of escape during quiet solar conditions?
4. Can inclusion of non-thermal escape in the model yield an estimation of water loss similar to the amount calculated in geomorphological studies?

To answer these questions, we have substantially upgraded our existing 1D photochemical model, now named bluejay, of the martian atmosphere. Spanning from the surface to 250 km, it now includes a self-consistent ionosphere with deuterated ions, fully couples the ions and neutrals without assumption of photochemical equilibrium, and has only argon as a fixed background species. To our knowledge, it is the first photochemical model to do all of this in the Mars literature.

Past photochemistry studies have typically used several simplifications which improve computational speed and make it easier to model the chemistry of ions and neutrals, which have very different timescales of chemical reaction. Most recent ion-neutral photochemical models use one or more of three common approaches: (1) a fixed (either wholly or partially) background neutral atmosphere (Fox et al., 2021, 2017, 2015; Matta et al., 2013;

Molina-Cuberos et al., 2002); (2) placing the lower boundary of the model near the bottom of the ionosphere (Fox et al., 2021; V. A. Krasnopolsky, 2019; Fox et al., 2015; Matta et al., 2013; V. A. Krasnopolsky, 2002); or (3) the assumption of photochemical equilibrium for chemically short-lived species (Vuitton et al., 2019; Banaszkiwicz et al., 2000) and/or neglect of ion diffusion (Dobrijevic et al., 2016). By building a model that does not use these approaches, we obtain a more complete understanding of the coupling of the lower to upper atmospheres, which has been recently shown to be key to understanding water transport, destruction, and escape during the Mars dusty season (Villanueva et al., 2021; Chaffin et al., 2021; Holmes et al., 2021; Stone et al., 2020; A. A. Fedorova et al., 2020; Vandaele et al., 2019; Aoki et al., 2019; Heavens et al., 2018). To accommodate the computational demands of the model, bluejay is built in Julia (Bezanson et al., 2017), a relatively new language designed specifically for numerical modeling.

We use our enhanced model to present the first theoretical analysis of D ion chemistry at Mars, which includes an updated quantification of non-thermal escape of D and H, the most critical reactions for production of hot H and D, and the implications for water loss.

2 Model description

Here we describe changes made to the 1D photochemical model as described by Cangi et al. (2020). In addition to the upgrades to physics and chemistry described below, this update incorporates computational improvements, such as extensive encapsulation, vectorization of functions, and performance tuning. The only species that we hold constant in our model is argon and lower atmospheric water (see Section 2.1.3).

The absolute tolerance is 1×10^{-12} , or 1 ppt, and the relative tolerance is 1×10^{-6} . If the percent change of a value is above relative tolerance, the model continues performing Newton iterations to predict the species densities at the next timestep, and stops once it falls below the relative tolerance. This becomes problematic when the values solved for are near machine precision (for 64-bit floats), as happens for ions in the lower atmosphere. In this scenario, the model relies on the absolute tolerance instead, which represents a level below which we do not demand any numerical accuracy; thus, densities that are below 1 ppt may be less representative of the real atmosphere than densities above.

2.1 New features

2.1.1 Ion reaction network

Our updated model contains ~ 600 total ion and neutral reactions. The deuterated reactions are shown in Table 1, and the non-deuterated reactions are available in Table S2; rate coefficients of H-analogue reactions are generally the same as those used by Cangi et al. (2020); Vuitton et al. (2019); Chaffin et al. (2017).

Scope of deuterated reactions: We define a deuterated analogue reaction as a reaction in which one H atom in one of the reactants has been replaced with D; for example, $D + O_2 \rightarrow DO_2$ instead of $H + O_2 \rightarrow HO_2$. We do not consider doubly deuterated reactions or species, e.g., we do not include reactions like $DO_2 + D \rightarrow OD + OD$ nor species like D_2O . The already very low relative abundance of D to H ($\sim 1 \times 10^{-3}$) means that doubly deuterated species and reactions will have an abundance lower by another factor of ~ 1000 , are thus expected to have a negligible effect on the atmospheric chemistry. Our deuterated reaction network includes all of the reactions shown in Table 1. The H-bearing analogues of the reactions in Table 1 contribute 99.99997% of the total column rate of all H-bearing reactions, meaning that most of the atmospheric chemistry of H has a deuterated analogue, so it is unlikely that we have accidentally biased our results against D production.

Table 1: Deuterated reactions used in the model. Reactions 1-6b: column rate ν in $\text{cm}^{-2}\text{s}^{-1}$. Reactions 7-125: rate coefficients in units of $\text{cm}^3 \text{molecule}^{-1} \text{s}^{-1}$ for bimolecular reactions and $\text{cm}^6 \text{molecule}^{-1} \text{s}^{-1}$ for termolecular reactions. BR = branching ratio; MS = mass scaling.

		Reaction	BR	MS	Rate coefficient	Ref
Photodissociation and photoionization						
1	D	$\rightarrow \text{D}^+$			$\nu_{\text{col}} = 7.5 \times 10^{-12}$	†
2	DO_2	$\rightarrow \text{OD} + \text{O}$			$\nu_{\text{col}} = 6.9 \times 10^{-8}$	†
3a	HD	$\rightarrow \text{HD}^+$			$\nu_{\text{col}} = 6.2 \times 10^{-12}$	†
3b		$\rightarrow \text{H} + \text{D}$			$\nu_{\text{col}} = 3.8 \times 10^{-12}$	†
3c		$\rightarrow \text{H}^+ + \text{D}$			$\nu_{\text{col}} = 6.9 \times 10^{-13}$	†
3d		$\rightarrow \text{D}^+ + \text{H}$			$\nu_{\text{col}} = 6.9 \times 10^{-13}$	†
4a	HDO	$\rightarrow \text{D} + \text{OH}$			$\nu_{\text{col}} = 4.4 \times 10^{-10}$	C0499
4b		$\rightarrow \text{H} + \text{OD}$			$\nu_{\text{col}} = 4.4 \times 10^{-10}$	C0499
4c		$\rightarrow \text{HD} + \text{O}(^1\text{D})$			$\nu_{\text{col}} = 5.6 \times 10^{-11}$	C0499
4d		$\rightarrow \text{HDO}^+$			$\nu_{\text{col}} = 3.3 \times 10^{-11}$	†
4e		$\rightarrow \text{OD}^+ + \text{H}$			$\nu_{\text{col}} = 6.4 \times 10^{-12}$	†
4f		$\rightarrow \text{OH}^+ + \text{D}$			$\nu_{\text{col}} = 6.4 \times 10^{-12}$	†
4g		$\rightarrow \text{D}^+ + \text{OH}$			$\nu_{\text{col}} = 2.9 \times 10^{-12}$	†
4h		$\rightarrow \text{H}^+ + \text{OD}$			$\nu_{\text{col}} = 2.9 \times 10^{-12}$	†
4i		$\rightarrow \text{O}^+ + \text{HD}$			$\nu_{\text{col}} = 3.8 \times 10^{-13}$	†
4j		$\rightarrow \text{H} + \text{D} + \text{O}$			$\nu_{\text{col}} = 0$	†
5a	HDO_2	$\rightarrow \text{OH} + \text{OD}$			$\nu_{\text{col}} = 1.1 \times 10^{-8}$	†
5b		$\rightarrow \text{DO}_2 + \text{H}$			$\nu_{\text{col}} = 3.1 \times 10^{-10}$	†
5c		$\rightarrow \text{HO}_2 + \text{D}$			$\nu_{\text{col}} = 3.1 \times 10^{-10}$	†
5d		$\rightarrow \text{HDO} + \text{O}(^1\text{D})$			$\nu_{\text{col}} = 0$	†
6a	OD	$\rightarrow \text{O} + \text{D}$			$\nu_{\text{col}} = 1.1 \times 10^{-9}$	NL84
6b		$\rightarrow \text{O}(^1\text{D}) + \text{D}$			$\nu_{\text{col}} = 1.6 \times 10^{-11}$	NL84
Deuterated neutral-neutral reactions						
7	$\text{CO} + \text{D}$	$\rightarrow \text{DCO}$			See text $k_{\infty} = 1 (T_n)^{0.2}$ $k_0 = 2.00 \times 10^{-35} (T_n)^{0.2}$	Est.
8a	$\text{CO} + \text{OD}$	$\rightarrow \text{CO}_2 + \text{D}$		$\sqrt{\frac{17}{18}}$	See text $k_{\infty} = 1.63 \times 10^{-6} (T_n)^{6.1}$ $k_0 = 4.90 \times 10^{-15} (T_n)^{0.6}$	Est.
8b		$\rightarrow \text{DOC O}$		$\sqrt{\frac{17}{18}}$	See text $k_{\infty} = 6.62 \times 10^{-16} (T_n)^{1.3}$ $k_0 = 1.73 \times 10^{-29} (T_n)^{-1.4}$	Est.
9	$\text{D} + \text{H}_2$	$\rightarrow \text{HD} + \text{H}$			$2.73 \times 10^{-17} (T_n)^{2.0} e^{-2700/T_n}$	NIST
10a	$\text{D} + \text{H}_2\text{O}_2$	$\rightarrow \text{H}_2\text{O} + \text{OD}$	0.5		$1.16 \times 10^{-11} e^{-2110/T_n}$	C10
10b		$\rightarrow \text{HDO} + \text{OH}$	0.5		$1.16 \times 10^{-11} e^{-2110/T_n}$	C10
11a	$\text{D} + \text{HO}_2$	$\rightarrow \text{DO}_2 + \text{H}$			1.00×10^{-10}	Y88
11b		$\rightarrow \text{HD} + \text{O}_2$			2.45×10^{-12}	Y88
11c		$\rightarrow \text{HDO} + \text{O}(^1\text{D})$			1.14×10^{-12}	Y88
11d		$\rightarrow \text{OH} + \text{OD}$			5.11×10^{-11}	Y88

Continued on next page

	Reaction	BR	MS	Rate or rate coefficient	Ref
				See text	
12	D + O ₂ → DO ₂		$\sqrt{\frac{1}{2}}$	$k_{\infty} = 2.40 \times 10^{-11} (T_n)^{0.2}$ $k_0 = 1.46 \times 10^{-28} (T_n)^{-1.3}$	Est.
13	D + O ₃ → OD + O ₂			$9.94 \times 10^{-11} e^{-470/T_n}$	NIST
14	D + OH + CO ₂ → HDO + CO ₂		$\sqrt{\frac{1}{2}}$	$1.16 \times 10^{-25} (T_n)^{-2.0}$	Est.
15	DCO + H → CO + HD		$\sqrt{\frac{29}{30}}$	1.50×10^{-10}	Est.
16a	DCO + O → CO + OD		$\sqrt{\frac{29}{30}}$	5.00×10^{-11}	Est.
16b	→ CO ₂ + D		$\sqrt{\frac{29}{30}}$	5.00×10^{-11}	Est.
17a	DCO + O ₂ → CO ₂ + OD		$\sqrt{\frac{29}{30}}$	7.60×10^{-13}	Est.
17b	→ DO ₂ + CO		$\sqrt{\frac{29}{30}}$	5.20×10^{-12}	Est.
18	DCO + OH → HDO + CO	0.5	$\sqrt{\frac{29}{30}}$	1.80×10^{-10}	Est.
19	DO ₂ + HO ₂ → HDO ₂ + O ₂		$\sqrt{\frac{33}{34}}$	$3.00 \times 10^{-13} e^{460/T_n}$	Est.
20	DO ₂ + N → NO + OD		$\sqrt{\frac{33}{34}}$	2.20×10^{-11}	Est.
21	DO ₂ + O ₃ → OD + O ₂ + O ₂		$\sqrt{\frac{33}{34}}$	$1.00 \times 10^{-14} e^{-490/T_n}$	Est.
22	DOC ₂ + O ₂ → DO ₂ + CO ₂		$\sqrt{\frac{45}{46}}$	2.09×10^{-12}	Est.
23	DOC ₂ + OH → CO ₂ + HDO		$\sqrt{\frac{45}{46}}$	1.03×10^{-11}	Est.
24	H + D + M → HD + M		$\sqrt{\frac{1}{2}}$	$6.62 \times 10^{-27} (T_n)^{-2.27}$	Est.
25a	H + DO ₂ → HD + O ₂		$\sqrt{\frac{33}{34}}$	3.45×10^{-12}	Est.
25b	→ HDO + O(¹ D)		$\sqrt{\frac{33}{34}}$	1.60×10^{-12}	Est.
25c	→ HO ₂ + D			$1.85 \times 10^{-10} e^{-890/T_n}$	Y88
25d	→ OH + OD		$\sqrt{\frac{33}{34}}$	7.20×10^{-11}	Est.
26	H + HD → H ₂ + D			$1.15 \times 10^{-11} e^{-3041/T_n}$	NIST
27a	H + HDO ₂ → H ₂ O + OD	0.5		$1.16 \times 10^{-11} e^{-2110/T_n}$	C10
27b	→ HDO + OH	0.5		$1.16 \times 10^{-11} e^{-2110/T_n}$	C10
28	H + OD + CO ₂ → HDO + CO ₂		$\sqrt{\frac{17}{18}}$	$1.16 \times 10^{-25} (T_n)^{-2.0}$	Est.
29	HCO + D → CO + HD		$\sqrt{\frac{1}{2}}$	1.50×10^{-10}	Est.
30	HCO + OD → HDO + CO	0.5	$\sqrt{\frac{29}{30}}$	1.80×10^{-10}	Est.
31a	HD + O → OD + H			$1.68 \times 10^{-12} e^{-4400/T_n}$	NIST
31b	→ OH + D			$4.40 \times 10^{-12} e^{-4390/T_n}$	NIST
32	HO ₂ + DO ₂ + M → HDO ₂ + O ₂ + M		$\sqrt{\frac{33}{34}}$	$4.20 \times 10^{-33} e^{920/T_n}$	Est.
33	HOCO + OD → CO ₂ + HDO		$\sqrt{\frac{17}{18}}$	1.03×10^{-11}	Est.
34	O + D → OD		$\sqrt{\frac{1}{2}}$	$8.65 \times 10^{-18} (T_n)^{-0.38}$	Est.
35	O + DO ₂ → OD + O ₂		$\sqrt{\frac{33}{34}}$	$3.00 \times 10^{-11} e^{200/T_n}$	Est.
36a	O + HDO ₂ → OD + HO ₂	0.5	$\sqrt{\frac{34}{35}}$	$1.40 \times 10^{-12} e^{-2000/T_n}$	Est.
36b	→ OH + DO ₂	0.5	$\sqrt{\frac{34}{35}}$	$1.40 \times 10^{-12} e^{-2000/T_n}$	Est.
37	O + OD → O ₂ + D		$\sqrt{\frac{17}{18}}$	$1.80 \times 10^{-11} e^{180/T_n}$	Est.
38a	O(¹ D) + HD → D + OH			4.92×10^{-11}	Y88
38b	→ H + OD			4.92×10^{-11}	Y88
39	O(¹ D) + HDO → OD + OH		$\sqrt{\frac{18}{19}}$	$1.63 \times 10^{-10} e^{60/T_n}$	Est.

Continued on next page

	Reaction	BR	MS	Rate or rate coefficient	Ref
40	OD + H → OH + D			$4.58 \times 10^{-9} (T_n)^{-0.63} e^{-717/T_n}$	Y88
41	OD + H ₂ → HDO + H			$2.80 \times 10^{-12} e^{-1800/T_n}$	Y88
42	OD + H ₂ O ₂ → HDO + HO ₂		$\sqrt{\frac{17}{18}}$	$2.90 \times 10^{-12} e^{-160/T_n}$	Est.
43	OD + HO ₂ → HDO + O ₂		$\sqrt{\frac{17}{18}}$	$4.80 \times 10^{-11} e^{250/T_n}$	Est.
44	OD + O ₃ → DO ₂ + O ₂		$\sqrt{\frac{17}{18}}$	$1.70 \times 10^{-12} e^{-940/T_n}$	Est.
45a	OD + OH → HDO + O		$\sqrt{\frac{17}{18}}$	1.80×10^{-12}	Est.
				See text	
45b	→ HDO ₂		$\sqrt{\frac{17}{18}}$	$k_\infty = 2.60 \times 10^{-11}$ $k_0 = 6.60 \times 10^{-29} (T_n)^{-0.8}$	Est.
46	OH + D → OD + H			$3.30 \times 10^{-9} (T_n)^{-0.63}$	Y88
47	OH + DO ₂ → HDO + O ₂		$\sqrt{\frac{33}{34}}$	$4.80 \times 10^{-11} e^{250/T_n}$	Est.
48a	OH + HD → H ₂ O + D			$4.20 \times 10^{-13} e^{-1800/T_n}$	Y88
48b	→ HDO + H			$5.00 \times 10^{-12} e^{-2130/T_n}$	S11
49a	OH + HDO ₂ → H ₂ O + DO ₂	0.5	$\sqrt{\frac{34}{35}}$	$2.90 \times 10^{-12} e^{-160/T_n}$	Est.
49b	→ HDO + HO ₂	0.5	$\sqrt{\frac{34}{35}}$	$2.90 \times 10^{-12} e^{-160/T_n}$	Est.
Deuterated ion-neutral reactions					
50	ArD ⁺ + CO → DCO ⁺ + Ar			1.25×10^{-9}	A03
51	ArD ⁺ + CO ₂ → DCO ₂ ⁺ + Ar			1.10×10^{-9}	A03
52a	ArD ⁺ + H ₂ → ArH ⁺ + HD			4.50×10^{-10}	A03
52b	→ H ₂ D ⁺ + Ar			8.80×10^{-10}	A03
53	ArD ⁺ + N ₂ → N ₂ D ⁺ + Ar			6.00×10^{-10}	A03
54	ArH ⁺ + HD → H ₂ D ⁺ + Ar			8.60×10^{-10}	A03
55a	Ar ⁺ + HD → ArD ⁺ + H			3.84×10^{-10}	A03
55b	→ ArH ⁺ + D			3.68×10^{-10}	A03
55c	→ HD ⁺ + Ar			4.80×10^{-11}	A03
56a	CO ₂ ⁺ + D → DCO ⁺ + O			6.38×10^{-11}	A03
56b	→ D ⁺ + CO ₂			2.02×10^{-11}	A03
57a	CO ₂ ⁺ + HD → DCO ₂ ⁺ + H	0.5	$\sqrt{\frac{2}{3}}$	2.35×10^{-10}	Est.
57b	→ HCO ₂ ⁺ + D	0.5	$\sqrt{\frac{2}{3}}$	2.35×10^{-10}	Est.
58a	CO ₂ ⁺ + HDO → DCO ₂ ⁺ + OH	0.5	$\sqrt{\frac{18}{19}}$	3.00×10^{-10}	Est.
58b	→ HCO ₂ ⁺ + OD	0.5	$\sqrt{\frac{18}{19}}$	3.00×10^{-10}	Est.
58c	→ HDO ⁺ + CO ₂		$\sqrt{\frac{18}{19}}$	1.80×10^{-9}	Est.
59	CO ⁺ + D → D ⁺ + CO			9.00×10^{-11}	A03
60a	CO ⁺ + HD → DCO ⁺ + H	0.25	$\sqrt{\frac{2}{3}}$	7.50×10^{-10}	Est.
60b	→ DOC ⁺ + H	0.25	$\sqrt{\frac{2}{3}}$	7.50×10^{-10}	Est.
60c	→ HCO ⁺ + D	0.25	$\sqrt{\frac{2}{3}}$	7.50×10^{-10}	Est.
60d	→ HOC ⁺ + D	0.25	$\sqrt{\frac{2}{3}}$	7.50×10^{-10}	Est.
61a	CO ⁺ + HDO → DCO ⁺ + OH	0.5	$\sqrt{\frac{18}{19}}$	8.40×10^{-10}	Est.
61b	→ HCO ⁺ + OD	0.5	$\sqrt{\frac{18}{19}}$	8.40×10^{-10}	Est.
61c	→ HDO ⁺ + CO		$\sqrt{\frac{18}{19}}$	1.56×10^{-9}	Est.
62	C ⁺ + HD → CH ⁺ + D	0.17		1.20×10^{-16}	A03

Continued on next page

	Reaction	BR	MS	Rate or rate coefficient	Ref
63a	$C^+ + HDO \rightarrow DCO^+ + H$	0.5	$\sqrt{\frac{18}{19}}$	$7.80 \times 10^{-9} (T_i)^{-0.5}$	Est.
63b	$\rightarrow DOC^+ + H$	0.5	$\sqrt{\frac{18}{19}}$	1.08×10^{-9}	Est.
63c	$\rightarrow HCO^+ + D$	0.5	$\sqrt{\frac{18}{19}}$	$7.80 \times 10^{-9} (T_i)^{-0.5}$	Est.
63d	$\rightarrow HDO^+ + C$			2.34×10^{-10}	Est.
63e	$\rightarrow HOC^+ + D$	0.5	$\sqrt{\frac{18}{19}}$	1.08×10^{-9}	Est.
64	$DCO_2^+ + CO \rightarrow DCO^+ + CO_2$		$\sqrt{\frac{45}{46}}$	7.80×10^{-10}	Est.
65a	$DCO_2^+ + e^- \rightarrow CO + O$	0.68		$4.62 \times 10^{-5} (T_i)^{-0.64}$	G05
65b	$\rightarrow CO + OD$	0.27		$4.62 \times 10^{-5} (T_i)^{-0.64}$	G05
65c	$\rightarrow CO_2 + D$	0.05		$4.62 \times 10^{-5} (T_i)^{-0.64}$	G05
66	$DCO_2^+ + H_2O \rightarrow H_2DO^+ + CO_2$		$\sqrt{\frac{45}{46}}$	2.65×10^{-9}	Est.
67	$DCO_2^+ + O \rightarrow DCO^+ + O_2$		$\sqrt{\frac{45}{46}}$	5.80×10^{-10}	Est.
68a	$DCO^+ + e^- \rightarrow CO + D$	0.92		$9.02 \times 10^{-5} (T_i)^{-1.1}$	GK
68b	$\rightarrow OD + C$	0.07		$9.02 \times 10^{-5} (T_i)^{-1.1}$	GK
69	$DCO^+ + H \rightarrow HCO^+ + D$			1.50×10^{-11}	A03
70	$DCO^+ + H_2O \rightarrow H_2DO^+ + CO$		$\sqrt{\frac{29}{30}}$	2.60×10^{-9}	Est.
71	$DOC^+ + CO \rightarrow DCO^+ + CO$		$\sqrt{\frac{29}{30}}$	6.00×10^{-10}	Est.
72	$DOC^+ + e^- \rightarrow OD + C$		$\sqrt{\frac{29}{30}}$	$1.19 \times 10^{-8} (T_i)^{1.2}$	Est.
73a	$DOC^+ + H_2 \rightarrow H_2D^+ + CO$	0.57		6.20×10^{-10}	A03
73b	$\rightarrow HCO^+ + HD$	0.43		6.20×10^{-10}	A03
74a	$D^+ + CO_2 \rightarrow CO_2^+ + D$			3.50×10^{-9}	A03
74b	$\rightarrow DCO^+ + O$			2.60×10^{-9}	A03
75	$D^+ + H \rightarrow D + H^+$	0.87		$6.50 \times 10^{-11} (T_i)^{0.5}$	Y89
76	$D^+ + H_2 \rightarrow H^+ + HD$			2.20×10^{-9}	A03
77a	$D^+ + H_2O \rightarrow H_2O^+ + D$			5.20×10^{-9}	A03
77b	$\rightarrow HDO^+ + H$	0.5	$\sqrt{\frac{1}{2}}$	8.20×10^{-9}	Est.
78	$D^+ + NO \rightarrow NO^+ + D$			1.80×10^{-9}	A03
79	$D^+ + O \rightarrow D + O^+$			2.80×10^{-10}	A03
80	$D^+ + O_2 \rightarrow O_2^+ + D$			1.60×10^{-9}	A03
81a	$H_2DO^+ + e^- \rightarrow H_2 + O$	0.5	$\sqrt{\frac{19}{20}}$	$9.68 \times 10^{-8} (T_i)^{-0.5}$	Est.
81b	$\rightarrow H_2O + D$	0.5	$\sqrt{\frac{19}{20}}$	$1.86 \times 10^{-6} (T_i)^{-0.5}$	Est.
81c	$\rightarrow HD + O$	0.5	$\sqrt{\frac{19}{20}}$	$9.68 \times 10^{-8} (T_i)^{-0.5}$	Est.
81d	$\rightarrow HDO + H$	0.5	$\sqrt{\frac{19}{20}}$	$1.86 \times 10^{-6} (T_i)^{-0.5}$	Est.
81e	$\rightarrow OD + H$	0.5	$\sqrt{\frac{19}{20}}$	$4.47 \times 10^{-6} (T_i)^{-0.5}$	Est.
81f	$\rightarrow OD + H_2$	0.5	$\sqrt{\frac{19}{20}}$	$1.04 \times 10^{-6} (T_i)^{-0.5}$	Est.
81g	$\rightarrow OH + D$	0.5	$\sqrt{\frac{19}{20}}$	$4.47 \times 10^{-6} (T_i)^{-0.5}$	Est.
81h	$\rightarrow OH + HD$	0.5	$\sqrt{\frac{19}{20}}$	$1.04 \times 10^{-6} (T_i)^{-0.5}$	Est.
82a	$H_2D^+ + CO \rightarrow DCO^+ + H_2$	0.33		1.60×10^{-9}	A03
82b	$\rightarrow HCO^+ + HD$	0.67		1.60×10^{-9}	A03
83a	$H_2D^+ + e^- \rightarrow H + H$	0.73		6.00×10^{-8}	L96
83b	$\rightarrow H_2 + D$	0.07		6.00×10^{-8}	L96
83c	$\rightarrow HD + H$	0.2		6.00×10^{-8}	L96

Continued on next page

	Reaction	BR	MS	Rate or rate coefficient	Ref
84	$\text{H}_2\text{D}^+ + \text{H}_2 \rightarrow \text{H}_3^+ + \text{HD}$			5.30×10^{-10}	A03
85a	$\text{H}_2\text{O}^+ + \text{HD} \rightarrow \text{H}_2\text{DO}^+ + \text{H}$	0.5	$\sqrt{\frac{2}{3}}$	3.80×10^{-10}	Est.
85b	$\rightarrow \text{H}_3\text{O}^+ + \text{D}$	0.5	$\sqrt{\frac{2}{3}}$	3.80×10^{-10}	Est.
86	$\text{HCO}_2^+ + \text{HDO} \rightarrow \text{H}_2\text{DO}^+ + \text{CO}_2$		$\sqrt{\frac{18}{19}}$	2.65×10^{-9}	Est.
87	$\text{HCO}^+ + \text{D} \rightarrow \text{DCO}^+ + \text{H}$			4.25×10^{-11}	A03
88	$\text{HCO}^+ + \text{HDO} \rightarrow \text{H}_2\text{DO}^+ + \text{CO}$		$\sqrt{\frac{18}{19}}$	2.60×10^{-9}	Est.
89a	$\text{HDO}^+ + \text{CO} \rightarrow \text{DCO}^+ + \text{OH}$	0.5	$\sqrt{\frac{18}{19}}$	2.12×10^{-10}	Est.
89b	$\rightarrow \text{HCO}^+ + \text{OD}$	0.5	$\sqrt{\frac{18}{19}}$	2.12×10^{-10}	Est.
90a	$\text{HDO}^+ + \text{e}^- \rightarrow \text{HD} + \text{O}$	0.1		1.50×10^{-7}	J99
90b	$\rightarrow \text{O} + \text{D}$	0.59		1.50×10^{-7}	J99
90c	$\rightarrow \text{OD} + \text{H}$	0.21		1.50×10^{-7}	J99
90d	$\rightarrow \text{OH} + \text{D}$	0.1		1.50×10^{-7}	J99
91a	$\text{HDO}^+ + \text{H}_2 \rightarrow \text{H}_2\text{DO}^+ + \text{H}$	0.5	$\sqrt{\frac{18}{19}}$	3.80×10^{-10}	Est.
91b	$\rightarrow \text{H}_3\text{O}^+ + \text{D}$	0.5	$\sqrt{\frac{18}{19}}$	3.80×10^{-10}	Est.
92a	$\text{HDO}^+ + \text{N} \rightarrow \text{HNO}^+ + \text{D}$	0.5	$\sqrt{\frac{18}{19}}$	5.60×10^{-11}	Est.
92b	$\rightarrow \text{NO}^+ + \text{HD}$		$\sqrt{\frac{18}{19}}$	2.80×10^{-11}	Est.
93	$\text{HDO}^+ + \text{NO} \rightarrow \text{NO}^+ + \text{HDO}$		$\sqrt{\frac{18}{19}}$	4.60×10^{-10}	Est.
94	$\text{HDO}^+ + \text{O} \rightarrow \text{O}_2^+ + \text{HD}$		$\sqrt{\frac{18}{19}}$	4.00×10^{-11}	Est.
95	$\text{HDO}^+ + \text{O}_2 \rightarrow \text{O}_2^+ + \text{HDO}$		$\sqrt{\frac{18}{19}}$	3.30×10^{-10}	Est.
96a	$\text{HD}^+ + \text{Ar} \rightarrow \text{ArD}^+ + \text{H}$	0.45	$\sqrt{\frac{2}{3}}$	2.10×10^{-9}	A03
96b	$\rightarrow \text{ArH}^+ + \text{D}$	0.55	$\sqrt{\frac{2}{3}}$	2.10×10^{-9}	Est.
97a	$\text{HD}^+ + \text{CO} \rightarrow \text{DCO}^+ + \text{H}$	0.5	$\sqrt{\frac{2}{3}}$	1.45×10^{-9}	Est.
97b	$\rightarrow \text{HCO}^+ + \text{D}$	0.5	$\sqrt{\frac{2}{3}}$	1.45×10^{-9}	Est.
98a	$\text{HD}^+ + \text{CO}_2 \rightarrow \text{DCO}_2^+ + \text{H}$	0.5	$\sqrt{\frac{2}{3}}$	1.17×10^{-9}	Est.
98b	$\rightarrow \text{HCO}_2^+ + \text{D}$	0.5	$\sqrt{\frac{2}{3}}$	1.17×10^{-9}	Est.
99	$\text{HD}^+ + \text{e}^- \rightarrow \text{H} + \text{D}$			$1.93 \times 10^{-6} (T_i)^{-0.853} e^{-43.3/T_i}$	KIDA
100	$\text{HD}^+ + \text{HD} \rightarrow \text{H}_2\text{D}^+ + \text{D}$			8.42×10^{-10}	A03
101a	$\text{HD}^+ + \text{N}_2 \rightarrow \text{N}_2\text{D}^+ + \text{H}$	0.5	$\sqrt{\frac{2}{3}}$	1.00×10^{-9}	Est.
101b	$\rightarrow \text{N}_2\text{H}^+ + \text{D}$	0.5	$\sqrt{\frac{2}{3}}$	1.00×10^{-9}	Est.
102a	$\text{HD}^+ + \text{O} \rightarrow \text{OD}^+ + \text{H}$	0.5	$\sqrt{\frac{2}{3}}$	7.50×10^{-10}	Est.
102b	$\rightarrow \text{OH}^+ + \text{D}$	0.5	$\sqrt{\frac{2}{3}}$	7.50×10^{-10}	Est.
103	$\text{HD}^+ + \text{O}_2 \rightarrow \text{HO}_2^+ + \text{D}$	0.5	$\sqrt{\frac{2}{3}}$	9.60×10^{-10}	Est.
104	$\text{H}^+ + \text{HD} \rightarrow \text{D}^+ + \text{H}_2$			1.10×10^{-10}	A03
105a	$\text{H}^+ + \text{HDO} \rightarrow \text{H}_2\text{O}^+ + \text{D}$	0.5	$\sqrt{\frac{18}{19}}$	8.20×10^{-9}	Est.
105b	$\rightarrow \text{HDO}^+ + \text{H}$	0.5	$\sqrt{\frac{18}{19}}$	8.20×10^{-9}	Est.
106	$\text{N}_2\text{D}^+ + \text{CO} \rightarrow \text{DCO}^+ + \text{N}_2$		$\sqrt{\frac{29}{30}}$	8.80×10^{-10}	Est.
107	$\text{N}_2\text{D}^+ + \text{e}^- \rightarrow \text{N}_2 + \text{D}$		$\sqrt{\frac{29}{30}}$	$6.60 \times 10^{-7} (T_i)^{-0.51}$	Est.
108	$\text{N}_2\text{D}^+ + \text{H} \rightarrow \text{N}_2\text{H}^+ + \text{D}$			2.50×10^{-11}	A03
109	$\text{N}_2\text{D}^+ + \text{O} \rightarrow \text{OD}^+ + \text{N}_2$		$\sqrt{\frac{29}{30}}$	1.40×10^{-10}	Est.

Continued on next page

	Reaction	BR	MS	Rate or rate coefficient	Ref
110	$\text{N}_2\text{H}^+ + \text{D} \rightarrow \text{N}_2\text{D}^+ + \text{H}$			8.00×10^{-11}	A03
111	$\text{N}_2^+ + \text{D} \rightarrow \text{D}^+ + \text{N}_2$			1.20×10^{-10}	A03
112a	$\text{N}_2^+ + \text{HD} \rightarrow \text{N}_2\text{D}^+ + \text{H}$	0.51		1.34×10^{-9}	A03
112b	$\rightarrow \text{N}_2\text{H}^+ + \text{D}$	0.49		1.34×10^{-9}	A03
113a	$\text{N}_2^+ + \text{HDO} \rightarrow \text{HDO}^+ + \text{N}_2$		$\sqrt{\frac{18}{19}}$	1.90×10^{-9}	Est.
113b	$\rightarrow \text{N}_2\text{D}^+ + \text{OH}$	0.5	$\sqrt{\frac{18}{19}}$	5.04×10^{-10}	Est.
113c	$\rightarrow \text{N}_2\text{H}^+ + \text{OD}$	0.5	$\sqrt{\frac{18}{19}}$	5.04×10^{-10}	Est.
114	$\text{N}^+ + \text{HD} \rightarrow \text{NH}^+ + \text{D}$	0.25		3.10×10^{-10}	A03
115	$\text{OD}^+ + \text{CO} \rightarrow \text{DCO}^+ + \text{O}$		$\sqrt{\frac{17}{18}}$	8.40×10^{-10}	Est.
116	$\text{OD}^+ + \text{CO}_2 \rightarrow \text{DCO}_2^+ + \text{O}$		$\sqrt{\frac{17}{18}}$	1.35×10^{-9}	Est.
117	$\text{OD}^+ + \text{e}^- \rightarrow \text{O} + \text{D}$		$\sqrt{\frac{17}{18}}$	$6.50 \times 10^{-7} (T_i)^{-0.5}$	Est.
118a	$\text{OD}^+ + \text{H}_2 \rightarrow \text{H}_2\text{O}^+ + \text{D}$	0.5	$\sqrt{\frac{17}{18}}$	9.70×10^{-10}	Est.
118b	$\rightarrow \text{HDO}^+ + \text{H}$	0.5	$\sqrt{\frac{17}{18}}$	9.70×10^{-10}	Est.
119	$\text{OD}^+ + \text{N} \rightarrow \text{NO}^+ + \text{D}$		$\sqrt{\frac{17}{18}}$	8.90×10^{-10}	Est.
120	$\text{OD}^+ + \text{N}_2 \rightarrow \text{N}_2\text{D}^+ + \text{O}$		$\sqrt{\frac{17}{18}}$	2.40×10^{-10}	Est.
121	$\text{OD}^+ + \text{O} \rightarrow \text{O}_2^+ + \text{D}$		$\sqrt{\frac{17}{18}}$	7.10×10^{-10}	Est.
122	$\text{OD}^+ + \text{O}_2 \rightarrow \text{O}_2^+ + \text{OD}$		$\sqrt{\frac{17}{18}}$	3.80×10^{-10}	Est.
123a	$\text{OH}^+ + \text{HD} \rightarrow \text{H}_2\text{O}^+ + \text{D}$		$\sqrt{\frac{2}{3}}$	9.70×10^{-10}	Est.
123b	$\rightarrow \text{HDO}^+ + \text{H}$		$\sqrt{\frac{2}{3}}$	9.70×10^{-10}	Est.
124	$\text{O}^+ + \text{D} \rightarrow \text{D}^+ + \text{O}$		$\sqrt{\frac{1}{2}}$	6.40×10^{-10}	Est.
125a	$\text{O}^+ + \text{HD} \rightarrow \text{OD}^+ + \text{H}$	0.46		1.25×10^{-9}	A03
125b	$\rightarrow \text{OH}^+ + \text{D}$	0.54		1.25×10^{-9}	A03
126	$\text{O}^+ + \text{HDO} \rightarrow \text{HDO}^+ + \text{O}$		$\sqrt{\frac{18}{19}}$	2.60×10^{-9}	Est.

†: Cross section assumed same as H-analogue. A03: Anicich (2003).

C0499: Cheng et al. (2004); Cheng et al. (1999). C10: Cazaux et al. (2010).

G05: Geppert et al. (2005). K09: Korolov et al. (2009). GK: Rate from K09, branching ratio from G05.

J99: Jensen et al. (1999). KIDA: Wakelam and Gratier (2019). L96: Larsson et al. (1996).

NIST: Manion et al. (2015). NL84: Nee and Lee (1984). S11: Sander et al. (2011).

Y88: Yung et al. (1988). Y89: Yung et al. (1989). Est: Estimated with mass scaling (see text).

Photodissociation and photoionization: Photodissociation and ionization of deuterated species is calculated using the solar spectrum (see Section 2.2.2), so the entry in the table under ‘Rate or rate coefficient’ represents the integrated column rate. The ‘Ref’ column refers to the source of the cross sections used. For photoionization cross sections of the H-analogue reactions, see Vuitton et al. (2019, and references therein).

Neutral and ion bimolecular and termolecular reactions: The rate coefficient used for a given reaction is the product of the ‘BR’, ‘MS’ and ‘Rate coefficient’ columns (empty fields are taken to be 1). ‘BR’, or branching ratio, accounts for the fact that deuteration of a reaction can create two or more branches with differing products where only one branch would exist for the H-analogue reaction. ‘MS’, or mass scaling, is a scaling factor equal to the square root of the mass ratio, $\sqrt{m_1/m_2}$, where m_2 is the mass of the deuterated species and m_1 the H-bearing species. This factor is applied to reactions for which we were not able to find a measurement in the literature to account for replace-

ment of one reactant H atom with one D atom; a similar approach was used previously by V. A. Krasnopolsky (2002) for reactions of neutral HD with dominant ions and minor H-bearing ions.

Most reactions in these tables proceed using the listed rate coefficients. A few exceptions apply; the categorization Types and formulae mentioned below are the same as used by Vuitton et al. (2019). A more complete description of the formulae used can be found in their Appendix B.

Reaction 7: Similar to its analogue $\text{CO} + \text{H} \rightarrow \text{HCO}$, this is a Type 4 (pressure dependent association) reaction. The Troe parameter for this reaction is 0, so we use the form:

$$k = k_R + \frac{(Mk_0k_\infty)}{Mk_0 + k_\infty} \quad (1)$$

Where k_R is 0 in this case and M is the background atmospheric density.

Reactions 8a, 8b, 12, and 45b: These are Type 6 ($\text{CO} + \text{OD} \rightarrow \text{CO}_2 + \text{D}$) and Type 5 ($\text{CO} + \text{OH} \rightarrow \text{DOC}$, $\text{D} + \text{O}_2 \rightarrow \text{DO}_2$, $\text{OD} + \text{OH} \rightarrow \text{HDO}_2$) pressure dependent bimolecular reactions, with the formulae originally given by J. Burkholder et al. (2019); Sander et al. (2011). We use the same forms here, but multiplied by our mass scaling factor.

Ion reactions which produce a lone D or H atom have the potential to cause the produced atom to be “hot”, that is, gaining enough excess energy from the reaction that they can escape. We describe this in more detail in Section 2.1.4.

2.1.2 Ambipolar diffusion

The model employs ambipolar diffusion for all ions, using the Langevin-Gioumousis-Stevenson equation (Bauer, 1973):

$$D_{ai} = \frac{k(T_i + T_e)}{m_i \sum \nu_{ij}} \quad (2)$$

$$\nu_{ij} = 2\pi \left(\frac{\alpha_j e^2}{\mu_{ij}} \right)^{1/2} n_j \quad (3)$$

Where D_{ai} is the ambipolar diffusion coefficient for ion i , ν_{ij} is the collision frequency of ion i with neutral j , α_j is the polarizability, e is the fundamental charge, and n is the neutral density. Polarizability values for neutrals are collected from Manion et al. (2015). Where polarizability was not available either in data or models for a deuterated species we include, we assumed the same value as the H-bearing analogue.

2.1.3 Partially fixed water profile

We assume a constant abundance of water in the lower atmosphere, which approximates the average water available due to seasonal cycles of polar cap sublimation and transport. The mixing ratio is 1.3×10^{-4} up to the hygropause; in our model (which does not include cloud microphysics), this is the point at which the water mixing ratio begins to follow the saturation vapor pressure curve. We take the hygropause to be 40 km, between 25 km by V. A. Krasnopolsky (2002) and its enhanced altitude of 50-80 km during dust storms (Heavens et al., 2018) and roughly in the middle of the cloud-forming region (Daerden et al., 2022; Neary et al., 2020). At 72 km, a minimum of saturation is reached; above that level, the abundance of water is a free variable. This allows a more holistic understanding of water and water ion chemistry in the upper atmosphere, which has been shown to be an important tracer of seasonal H escape (Stone et al., 2020). The total amount

of water in the atmosphere is 10.5 precipitable μm , in accordance with observations (Smith, 2004; ?, ?).

2.1.4 *Non-thermal escape*

Although there are many non-thermal escape mechanisms, in this work, we focus on photochemical loss, i.e. the contribution to escape from chemistry and photochemistry. We neglect processes involving the solar wind such as sputtering, ion pickup, and charge exchange with the solar wind. Processes which depend upon the solar wind will primarily occur above the bow shock (which is far above our top boundary), where the solar wind can interact with the corona before being mostly deflected around the planet (Halekas et al., 2017). By focusing on planetary ionospheric reactions, we capture the non-thermal escape of H and D sourced from the atmosphere below the exobase.

We calculate the non-thermal escape of hot atoms created via ion-neutral chemistry as the product of the probability of escape and the volume production rate of hot atoms using the procedure described by Gregory, Elliott, et al. (2023), using the collisional cross sections for D and H on O (lacking data on collision with CO_2) by Zhang et al. (2009). We have evaluated all ion-neutral reactions that produce H, D, H_2 , or HD in the model for their exothermicity ($\Delta H_{\text{f,products}}^{\circ} - \Delta H_{\text{f,reactants}}^{\circ}$, following Fox (2015)) and only use those where the excess energy, equal to the difference in enthalpies of products and reactants, is positive and exceeds the energy required for H or D to escape to space. In reality, varying amounts of the excess heat produced can contribute to electronic and/or rovibrational excitations of the more massive second product molecule. A detailed analysis of these energy branches is beyond the scope of this work, in which we provide a first look at these reactions, so we neglect branching of energy into the non-H or D product, and assume that all excess energy ends up in the atomic H or D (see the Supporting Information). We use the escape probability curve calculated by Gregory, Elliott, et al. (2023) for an H atom of excess energy 5 eV; this is a reasonable approximation of the actual mean excess energy in our model, which is 3.6 eV. At this time, escape probabilities for larger atoms and molecules have not been calculated, so we also apply the escape probability to D, H_2 , and HD. We expect this may introduce no more than a few percent uncertainty in our calculation of the escape of these species. A more rigorous analysis of energy branching ratios and their effect on escape, as well as an update with probability curves for D, H_2 , and HD, is a worthy subject for future work.

The resulting volume escape rate can be integrated to obtain an escape flux for the top boundary of the model. Although our focus is escape of atomic H and D, some loss does occur via loss of the molecular form, so we also include non-thermal escape of H_2 and HD. In these cases, we assume that σ_{H_2} is the same as for D due to the similar masses, and that σ_{HD} is larger than H_2 by the same amount that D is larger than H. Although this is not an ideal assumption if one is interested in highly accurate non-thermal H_2 and HD escape, it is acceptable for our purposes, as that escape is very small compared to atomic escape of H and D.

2.2 Model inputs

Because the importance of non-thermal escape is expected to vary with solar activity, we have constructed three sets of inputs representing solar minimum, mean, and maximum conditions. The only properties which we vary between these cases are the neutral exobase temperatures and the incoming solar flux. Figure 1 shows these inputs in the navy, purple, and yellow colors. The inputs represent a dayside mean atmosphere (solar zenith angle $[\text{SZA}] = 60^\circ$).

2.2.1 *Atmospheric temperature profiles*

Standard neutral temperatures were obtained from the Mars Climate Database (Millour & Forget, 2018) by several layers of averaging, in order of first to last: by longitude, local time (9, 12, and 3 pm local times, night excluded), latitude (weighted by encompassed surface area), and L_s . Over the solar cycle, the only significant change is to the exobase

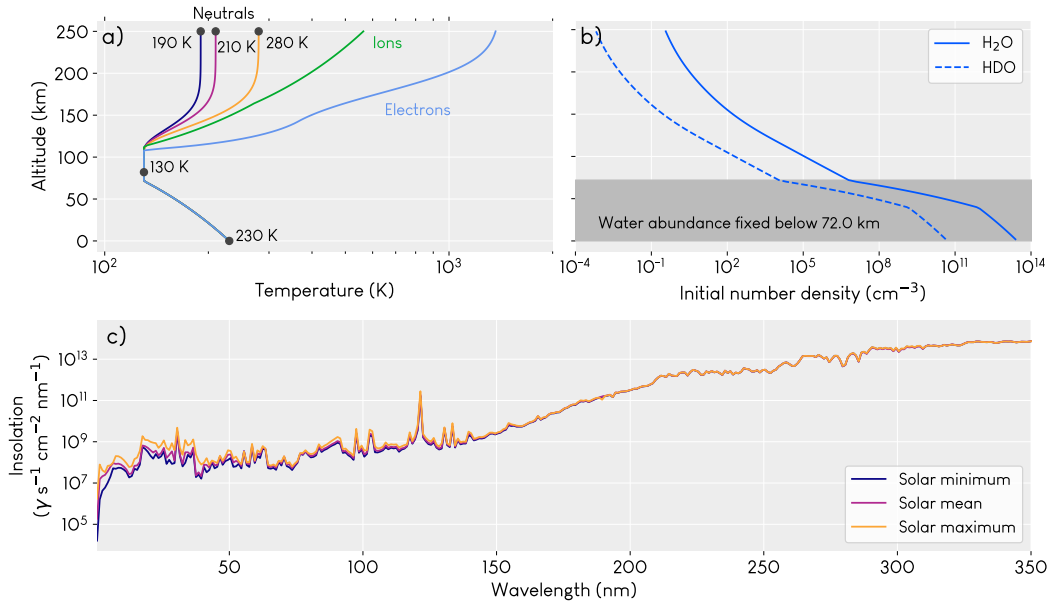


Figure 1. Main model inputs. a) Temperature profiles, with separate neutral exobase temperatures for each solar condition. Ion and electron temperatures are fits to data from MAVEN/STATIC as reported by Hanley et al. (2022) and MAVEN/LPW as reported by Ergun et al. (2015). b) Initial water profile. Above 72 km, water densities evolve according to the chemistry and transport. c) Insolation profiles from 0-350 nm for solar minimum, mean, and maximum. The full input spectrum goes out to 2400 nm, but the insolation there is relatively flat, with no variation due to solar cycle.

temperature, so we hold the surface and mesospheric temperature constant at 230 K and 130 K respectively.

In order to support modeling of ion chemistry, we use a piecewise fit to the new ion temperature profiles obtained at $\text{SZA}=60^\circ$ with the STATIC instrument by Hanley et al. (2022). These new data have overturned long-standing assumptions that the neutrals, ions, and electrons thermalize to the same temperature around 125 km (Schunk & Nagy, 2009), and thus represent a significant update in Mars photochemistry. We also include a fit to the electron profile from the Mars Atmosphere and Volatile EvolutionN mission (MAVEN) Langmuir Probes and Waves (LPW) instrument (Ergun et al., 2015). Because it is difficult to associate ion temperatures with contemporary neutral temperatures due to the averaging required for the neutral profiles, and because the data are limited in time, we do not change the ion or electron profiles for the different solar cycle scenarios. Past work indicates relatively minor temperature differences due to solar cycle (Kim et al., 1998); further analysis of MAVEN STATIC data provides an opportunity to confirm or deny this. Any variation with solar cycle is likely to have a minor impact on our results.

2.2.2 Insolation

Incoming solar photons are key reactants in photochemical reactions. For each solar case, we include photon fluxes from 0.5–2400 nm, binned in 1 nm increments. Total flux, once obtained, is scaled to Mars’ orbit and $\text{SZA}=60^\circ$.

We determined the dates of recent representative solar conditions by looking for periods when Ly α irradiance in the Lyman-alpha Model Solar Spectral Irradiance data set (Woods et al., 2019) reached a peak, average, or trough. Because solar maximum and

mean in recent decades have been historically quiet, we chose dates from the early 2000s to get a more representative photon flux for maximum and mean (solar minimum has not changed much). The dates we used were February 25, 2019 for solar minimum; February 7, 2004 for mean; and March 22, 2002 for maximum.

For the insolation flux data, we use *SORCE/SOLSTICE* at solar minimum and mean, and a mix of *SORCE/SOLSTICE* and *TIMED/SEE* at solar maximum. There is an additional complication for solar maximum: *SORCE/SOLSTICE* began a year after our solar maximum date, but includes the longer wavelengths we need, while *TIMED/SEE* began before our solar maximum date, but only includes fluxes at wavelengths shortwards of 190 nm. We patched together these two datasets, using *SORCE/SOLSTICE* for wavelengths 190-2000 nm from June 4, 2015 and *TIMED/SEE* for wavelengths 0.5-189.5 nm from March 22, 2002.

Figure 1a shows the fluxes only from 0.5 to 300 nm for simplicity; longwards of 350 nm, the profile does not vary over the solar cycle. The region shortward of 350 nm is also more important for photochemistry as the photodissociation and photoionization cross sections are largest there. We use the same cross sections as Cangi et al. (2020), with the addition of new photoionization and a few neutral photodissociation cross sections, the same used by Vuitton et al. (2019).

2.3 Boundary conditions

We use mostly the same boundary conditions as Cangi et al. (2020). The key addition is an additional non-thermal flux boundary condition at the top of the model for H, D, H₂, and HD, according to the functional form described by (Gregory, Elliott, et al., 2023). Flux is zero at the top and bottom of the model for all ion species and any neutral species without a different boundary condition.

It is worth emphasizing that our flux boundary condition at the top of the model for atomic O is fixed at $1.2 \times 10^8 \text{ cm}^{-2}\text{s}^{-1}$. This value has been used in past work (Nair et al., 1994) to ensure that equilibrium models would produce H escape rates similar to that calculated from Mariner data. Results from MAVEN (Dong et al., 2015; Leblanc et al., 2015; Brain et al., 2015; Lillis et al., 2017; Jakosky et al., 2018) indicate a present-day total O escape of closer to $3.8 \times 10^7 \text{ cm}^{-2}\text{s}^{-1}$. We retain the use of $1.2 \times 10^8 \text{ cm}^{-2}\text{s}^{-1}$ in this work, but in future work will explore the effect of the lower MAVEN-derived loss rates on H and D escape.

3 Results

3.1 What are the atmospheric densities of deuterated ions?

The general distribution of the deuterated ionospheric species is similar to that of their H-analogues. Vertical profiles for select species containing H or D are shown in Figure 2. Although they are calculated from surface to 250 km, the figure's lower boundary is placed at 80 km for legibility. The full image from surface to 250 km showing all species in the model appears in the Supporting Information (Figure S1).

Primary peaks in the densities of deuterated ions occur between 150 and 200 km, with a minor peak near the top of the mesosphere, around 90-125 km. This structure does not hold for all species. H₃O⁺ has its peak much lower down at about 90 km, which is in agreement with previous modeling (Fox et al., 2015; Molina-Cuberos et al., 2002). Unfortunately, comparisons with data are not feasible at this altitude because such data do not exist. Most ionic species, H- and D-bearing alike, also display a slight dip in density around 150 km, which is caused by a feature of the same shape in the electron temperature profile (see Figure 1a).

At solar maximum, greater insolation at short wavelengths enables more photoionization, increasing the abundances of primary species CO₂⁺, O₂⁺, and O⁺ which are produced directly from the parent neutrals. But for the lighter (and often more minor) ions

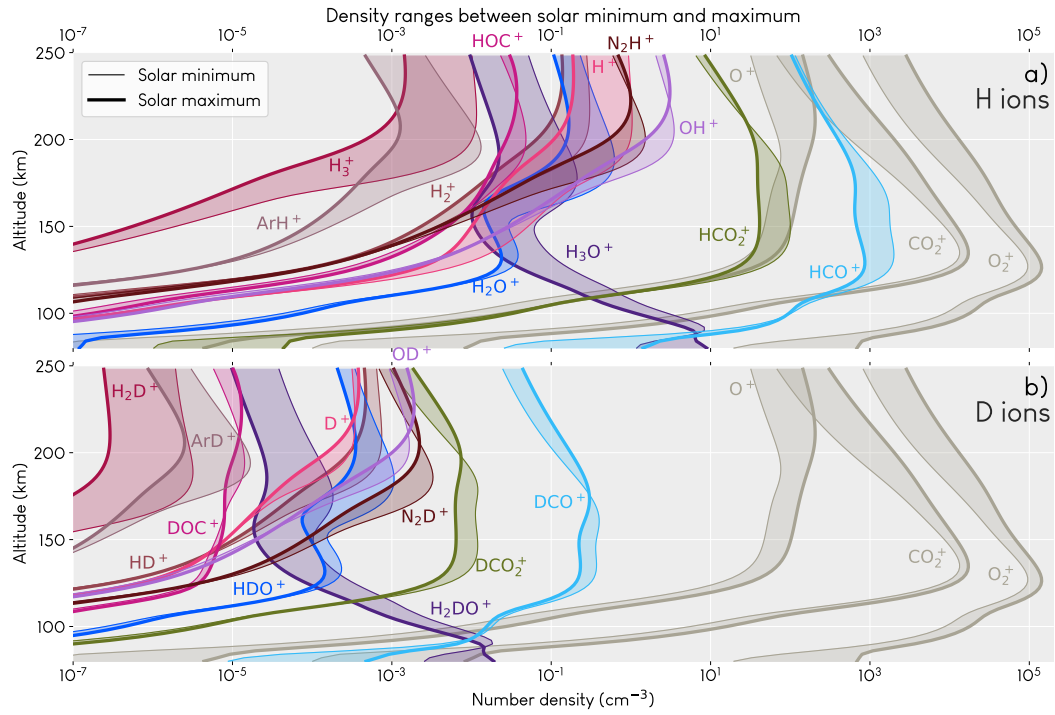


Figure 2. Densities of a) H-bearing ions and b) D-bearing (deuterated). Density ranges are bounded by their values at solar minimum (thin line) and solar maximum (thick line), with solar mean values falling within the shaded area. Gray lines show the primary ionospheric species for comparison.

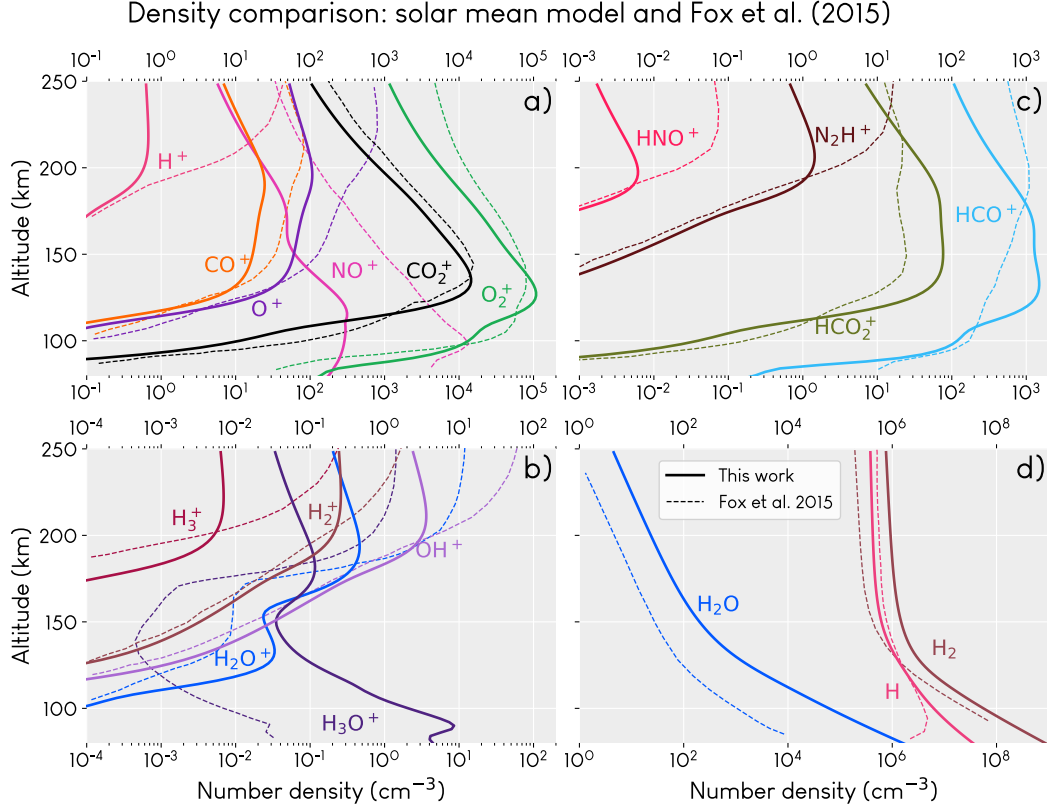


Figure 3. Ion and neutral densities computed by our model and compared with those computed by Fox et al. (2015). Species are divided amongst the four panels for legibility and compared with Figure 3 in Fox et al. (2015). Some minor species are omitted for clarity.

containing H and D, chemistry and/or transport is a more important driver than photoionization. Temperature-driven changes in the parent neutral densities propagate through to their ions; for example, H^+ abundance at the top of the atmosphere decreases as the temperature goes up because H escape is diffusion-limited, whereas the same is not true for D abundance (Cangi et al., 2020; Zahnle et al., n.d.). For other minor species that are not diffusion-limited, higher temperatures can also stimulate faster chemical reactions, slightly enhancing production and therefore density at higher temperatures.

3.1.1 Comparisons with previous works

Here, we compare our results to modeling results by Fox et al. (2015, 2021) and measurements by MAVEN NGIMS (Benna et al., 2015; Fox et al., 2021). In this work, we have parameterized our atmosphere in order to obtain an understanding of the mean-field behavior in time and space. We have not attempted to match the same modeling input or the relevant atmospheric conditions of those studies. Our models differ substantially from those by Fox et al. (2021, 2015) in temperature structure, boundary conditions (especially for ions at the upper boundary), vertical extent, use of photochemical equilibrium, background atmosphere, SZA, included species, mean Mars-Sun distance, assumed eddy diffusion profile, and included processes (we do not model electron impact ionization or dissociation). Because of these differences, we provide these comparisons primarily for the reader’s orientation.

Fox et al. (2015). For the major ions such as O^+ , CO_2^+ , and O_2^+ , our density profiles are generally consistent with those modeled by Fox et al. (2015), as shown in Fig-

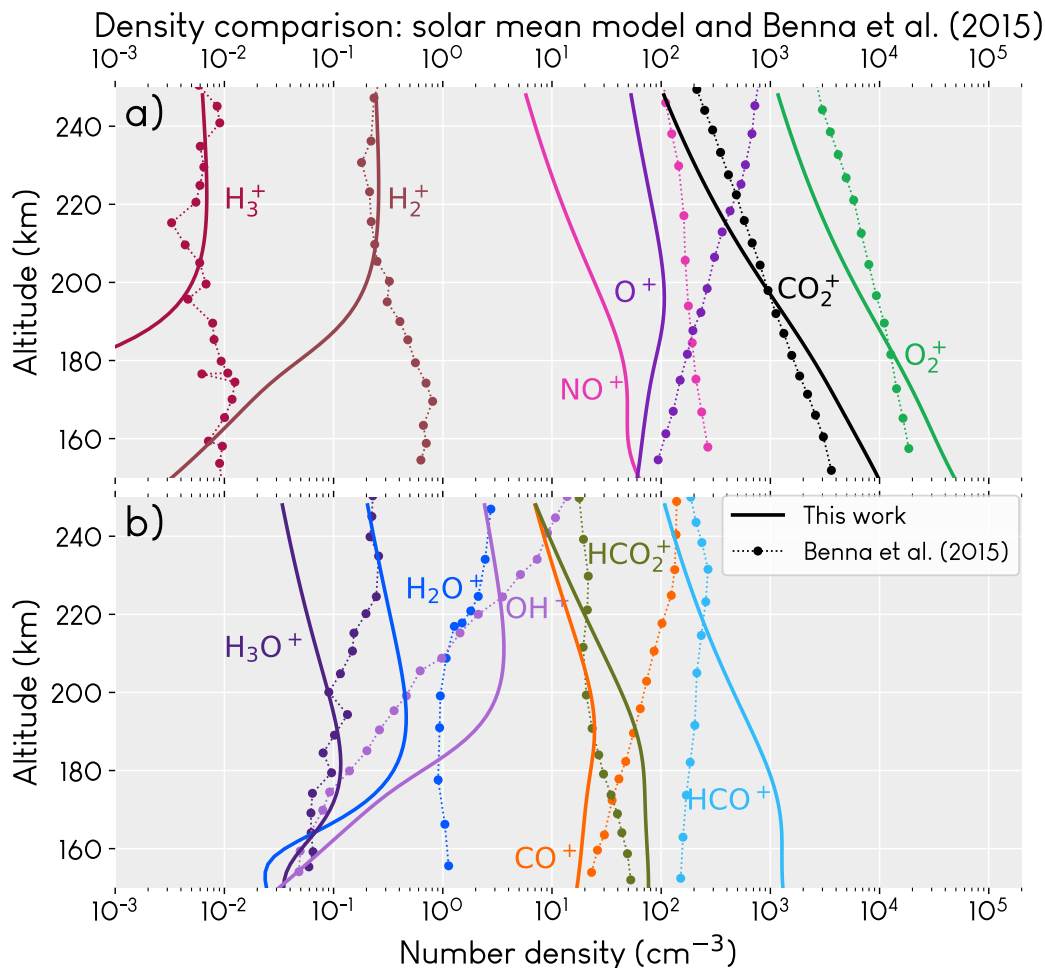


Figure 4. Ion and neutral densities computed by our model and compared with those computed by Benna et al. (2015). Species are divided amongst the two panels for legibility. HNO⁺ differs significantly from data and has been omitted; the measurements are known to be unreliable due to spacecraft potential.

ure 3. They are also broadly similar for many of the minor ions, although in general, our profiles tend to show lower densities near 250 km by 1-2 orders of magnitude. There is a significant difference between our NO⁺ profiles, which likely relates to differences between this work and that of Fox et al. (2015) in the nitrogen ion chemistry and included species. It should be noted that many of the ions for which we show a significantly different profile are quite minor, with populations never exceeding 100 cm⁻³, so the absolute differences as a percent of the total atmosphere are tiny, well within the absolute tolerance. Fox et al. (2015) make the point that their model calculates neutral H₂O produced only by ion-neutral reactions due to their choice of boundary conditions, whereas ours includes production by photodissociation and lower atmospheric neutral chemistry; it is then perhaps not surprising that our results include more water and different distributions of water-group ions and H-bearing species than theirs (see Figure 3d).

In Figure S3, we also compare our results to Fox et al. (2021), which uses a similar model to Fox et al. (2015) and includes recent data from NGIMS for CO₂⁺, O₂⁺ and O⁺. Compared to that paper, our results are more dissimilar.

Benna et al. (2015), using MAVEN NGIMS. Figure 4 shows that our results are in reasonably good agreement with the initial NGIMS measurements at Mars (Benna et al., 2015), which occurred long enough into the mission that solar mean conditions would have prevailed. There continues to be a divergence between model and data for O^+ in the upper atmosphere and an underprediction of NO^+ , but considering we are using a 1D model that does not account for local and short-term variations and we have not made any model changes to match data, we find the output acceptable. Significant differences in minor H-bearing ions have a variety of explanations here. NGIMS has background noise typically at 0.01 cm^{-3} and below, and a random uncertainty of 50% at 0.1 cm^{-3} (Benna et al., 2015), which may explain the divergence in H_3^+ and H_2^+ ; this difference could also result from the larger amount of the principal H_2O^+ ion present in the data. H_2^+ and H_3^+ are also measured in the lowest mass channels that the instrument can access, where the instrument is less sensitive due to a correlation of sensitivity with cross section; there is also a possibility of H outgassing from the instrument filament (Mahaffy et al., 2015).

3.2 Are the dominant production mechanisms of hot H and D analogous or dissimilar?

Figure 5 shows the production mechanisms for hot H and D, which are mostly similar. The hot H production mechanisms are also calculated independently by Gregory, Chaffin, et al. (2023, this issue).

The most important reaction driving the production of hot D (H) below 200 km in solar mean and maximum is $DCO^+(HCO^+)$ dissociative recombination (DR), with $CO_2^+ + HD (H_2)$ a close second. HCO^+ DR dominates for hot H under all solar conditions, but for hot D, $CO_2^+ + HD$ marginally dominates over DCO^+ DR during solar minimum at certain altitudes, making it the dominant source of escaping hot D at solar minimum. This is because the density of HD relative to DCO^+ is larger than H_2 relative to HCO^+ . The rates of production from these two processes for hot D are very close; minor changes in conditions, including normal fluctuations in the real atmosphere, could likely change this relationship. Above 200 km, $CO_2^+ + H_2$ dominates for hot H production, but high-altitude hot D comes mostly from $O^+ + HD$.

$DCO_2^+(HCO_2^+)$ DR is the third most important reaction during quiet solar conditions, but it is eclipsed by $O^+ + HD (H_2)$ during solar maximum. Under quieter solar conditions, the fifth place position is seized by $N_2^+ + HD (H_2)$. But as the thermosphere warms, OD (OH) + O claims the fifth place, first for the H species and then for the D species. This appears to be because the dominant reaction involving OH^+ and OD^+ is the reaction $O^+ + H_2 (HD) \rightarrow OH^+(OD^+) + H$. This reaction also has a rate coefficient that is independent of temperature, whereas $N_2^+ + HD (H_2)$ has a rate coefficient which decreases with temperature.

3.3 What is the magnitude of non-thermal escape of D, and under which conditions does it dominate thermal escape?

Figure 6 shows the relative contributions of thermal and non-thermal escape of atomic H and D and thermal escape of the molecular species; the associated escape fluxes to space are given in Table 2. The density profiles of the neutral species, from which the escape is sourced, appear in Figure S2; an upcoming publication will focus on variations in these neutral species and their D/H ratios. As in previous work, (e.g. V. A. Krasnopolsky, 2002), thermal escape is the dominant loss process for atomic H, with non-thermal escape of H making up a gradually reducing share as solar activity increases. The picture looks very different for D, for which 62-99.3% of escape is non-thermal depending on solar conditions. Note that, as shown in Table 2, the total escape of H and D adds to $2.4 \times 10^8 \text{ cm}^{-2}\text{s}^{-1}$ under all solar conditions due to the boundary condition on O escape. H and O escape are linearly related when the atmosphere is in equilibrium: the sum $\phi_H + \phi_D$ will naturally evolve to equal twice the O escape flux, since H_2O and HDO are the pri-

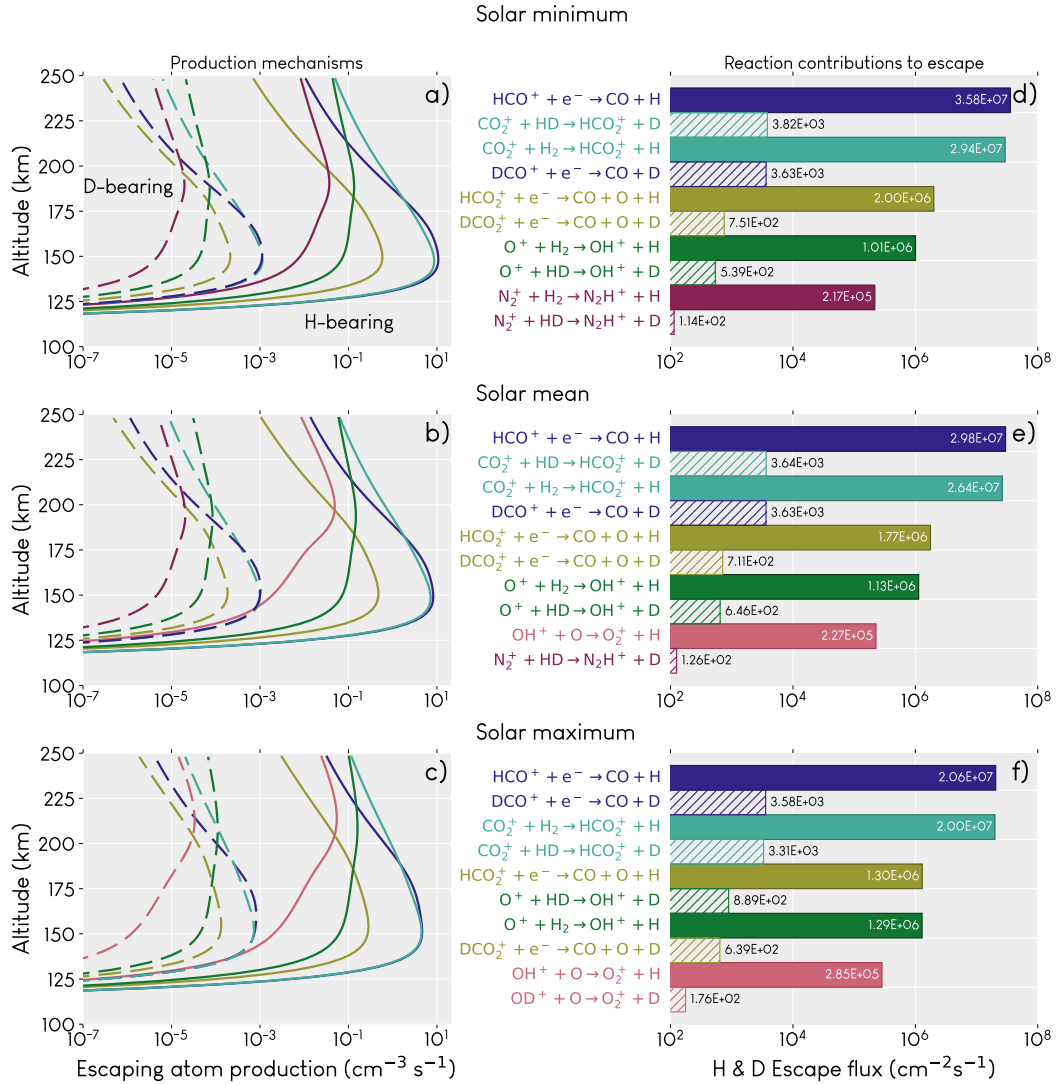


Figure 5. Volume production rates of escaping atoms (panels a, b, c) and integrated escape flux of the produced atomic H or D (d, e, f) for the dominant five chemical pathways producing hot H (solid lines/solid bars) and hot D (dashed lines/striped bars).

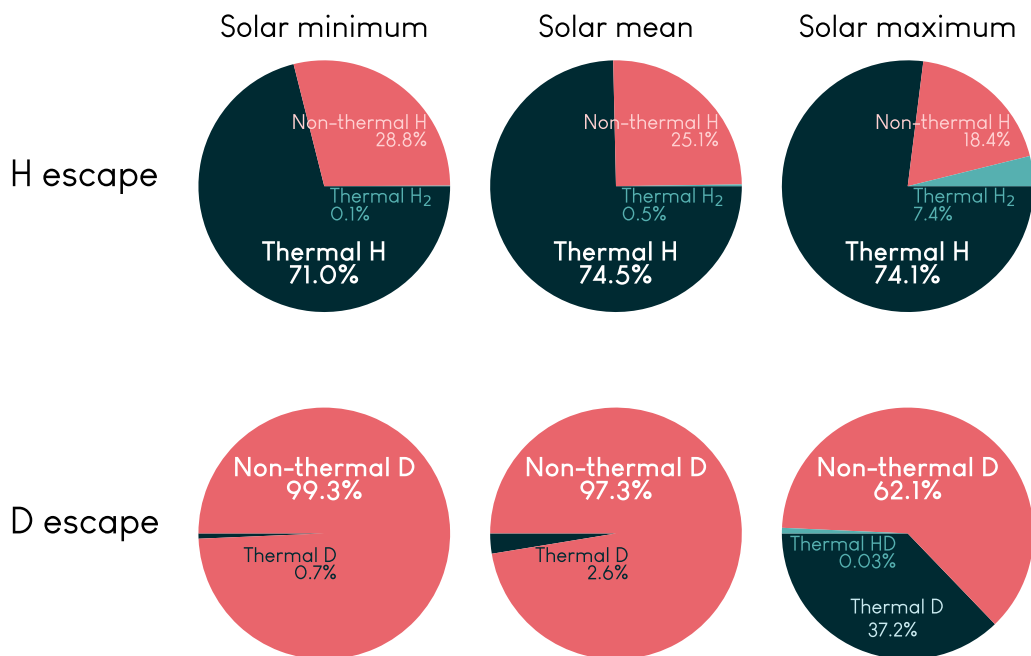


Figure 6. Relative escape contributions for H and D. As expected based on the literature, thermal escape dominates for H during all solar conditions, but non-thermal escape dominates D escape, even at solar maximum. Although we do model non-thermal escape of H_2 and HD, their contributions are completely negligible (see Table 2).

primary source of H and D in the model, and contain two H or D for every O. This relation does not necessarily hold over shorter timescales, when short-term perturbations can temporarily break this stoichiometric equilibrium.

Previous work has predicted that thermal escape of D should actually dominate at solar maximum (V. A. Krasnopolsky, 2002) and that non-thermal escape of D in the form of larger molecules such as HD, OD, and HDO could be up to 15% (Gacesa et al., 2018), whereas our results show that non-thermal escape of HD is so negligible as to not appear at all in Figure 6. Besides the fact that we do not account for excited rotational states of HD, the discrepancy also likely arises from our chosen methods. Our non-thermal escape probability curve is valid for hot H atoms with 5 eV of energy, and we do not account at all for branching to excited internal states of the other products; we assume that all atomic H and D produced by exothermic reactions are produced “hot”. In reality, not all exothermic heat is dumped directly into the lone atoms all the time. With proper accounting for these intricate branching ratios, our calculated total of non-thermally escaping atomic D would likely decrease. We also do not calculate non-thermal OD escape, as escape probabilities for a molecule of this mass are not available.

4 Discussion

Figure 7 places our D and H densities in context with other studies. We have only consolidated reported densities; we make no attempt to filter by observation geometries. Nevertheless, there appears to be an inverse relationship of densities and temperature for both species. We can also see that photochemical models (red/purple/pink points) produce D densities that are an order of magnitude smaller than densities retrieved using observations and radiative transfer modeling; the same discrepancy does not occur for the H densities. Deuterium Lyman α is difficult to separate from hydrogen Lyman α ;

	Thermal escape ($\text{cm}^{-2}\text{s}^{-1}$)				Non-thermal escape ($\text{cm}^{-2}\text{s}^{-1}$)				Total escape ($\text{cm}^{-2}\text{s}^{-1}$)		
	H	D	H ₂	HD	H	D	H ₂	HD	H	D	H + D
Solar minimum	1.70×10^8	62	1.66×10^5	0.1	6.92×10^7	9225	11871	7	2.39991×10^8	9295	2.4×10^8
Solar mean	1.79×10^8	243	5.43×10^5	0.9	6.02×10^7	9154	9491	7	2.39991×10^8	9405	2.4×10^8
Solar maximum	1.78×10^8	5415	8.92×10^6	104	4.43×10^7	9041	5473	4	2.39985×10^8	14564	2.4×10^8

Table 2. Amount of thermal and non-thermal escape of atomic and molecular H and D species for the three solar conditions. The total escape amounts to $2.4 \times 10^8 \text{ cm}^{-2}\text{s}^{-1}$ because in the equilibrium atmosphere, the ratio ϕ_H/ϕ_O approaches 2, as O escape is fixed at $1.2 \times 10^8 \text{ cm}^{-2}\text{s}^{-1}$ (see Section 2.3). Escaping atoms and molecules are sourced from the neutral species; densities for the associated species are shown in Figure S2.

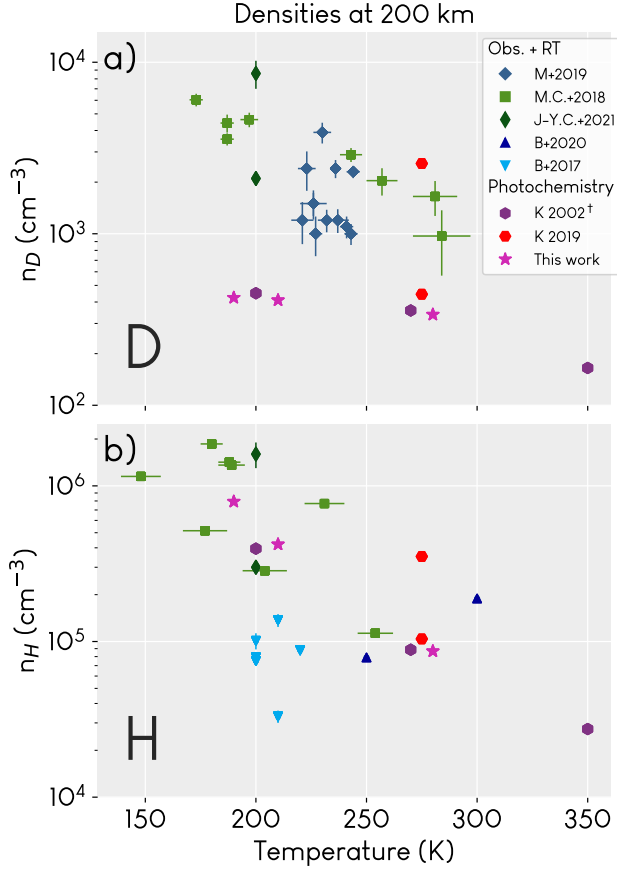


Figure 7. D and H densities at 200 km ([†] 250 km) from multiple studies. Data represent multiple solar zenith angles, seasons, hemispheres, etc. M+2019: Mayyasi et al. (2019). M.C.+2018: Chaffin et al. (2018). J-Y.C.+2021: Chaufray, Mayyasi, et al. (2021). B+2020, 2017: Bhattacharyya et al. (2020, 2017). K 2002, 2019: V. A. Krasnopolsky (2002, 2019). Entries under “Obs. + RT” used brightness observations from either HST (Bhattacharyya et al., 2017) or MAVEN IUVS (all others) with radiative transfer modeling for density retrievals. For these studies, invisible density error bars indicate uncertainty smaller than the marker size. Temperature error bars indicate that temperature was retrieved from spacecraft data, while missing temperature error bars mean it was a model parameter or output. Uncertainties for photochemistry studies are not calculated. Photochemical modeling typically reports an order of magnitude less D than other methods, which may be due to observation biases toward times of brighter D emission. There is no similar discrepancy in H densities.

the D density discrepancy may potentially be explained by a systematic bias toward anomalously bright D emissions. One exception is the density of D at ~ 2500 and $T=275\text{K}$ in the work by V. A. Krasnopolsky (2019); this point represents a model run with a high amount of water in the thermosphere, whereas all the other photochemical results have a comparatively lower water abundance. This comparison demonstrates that our model output is in reasonable agreement with other works.

As mentioned previously, we do not include cloud or dust microphysics, although these processes do have an important effect on the water cycle. These effects are explored in two recent papers using the Laboratoire de Météorologie Dynamique Planetary Climate Model (LMD-PCM) to study the creation of water ice clouds and their role in controlling the D/H ratio (Vals et al., 2022; Rossi et al., 2022).

4.1 Can inclusion of non-thermal escape in the model yield an estimation of water loss similar to the amount calculated in geomorphological studies?

By considering both thermal and non-thermal escape, we can now compute the D/H fractionation factor, which represents the relative efficiency of D and H escape. It is defined as:

$$f = \frac{\phi_D/\phi_H}{[\text{HDO}]_s/2[\text{H}_2\text{O}]_s} \quad (4)$$

Where $\phi_X = \phi_{X,t} + \phi_{X,n}$ is the rate at which species X (D or H) escapes from the top of the atmosphere due to both thermal (t) and non-thermal (n) processes. The denominator represents the D/H ratio in water measured at the surface (s), which is a proxy for the D/H ratio in the larger exchangeable reservoir.

The fractionation factor is important not only because it tells us how efficient loss of D is compared to loss of H, but also because it is useful for calculating the integrated water loss from a planet. Long-term enrichment of the heavy isotope (D) due to differential escape of D and H can be modeled using Rayleigh fractionation (Chamberlain & Hunten, 1987; Yung & DeMore, 1998):

$$\frac{(\text{D}/\text{H})_{\text{now}}}{(\text{D}/\text{H})_{\text{past}}} = \left(\frac{[\text{H}]_{\text{past}}}{[\text{H}]_{\text{now}}} \right)^{1-f} \quad (5)$$

Equation 5 is used to calculate water loss from Mars. The D/H ratio on the left hand side represents the ratio measured in water in the exchangeable reservoir (the seasonal polar caps, near-surface ices, and atmospheric water vapor), and the ratio $\text{H}_2\text{O}_{\text{past}}/\text{H}_2\text{O}_{\text{now}}$ can be substituted in on the righthand side and rearranged, obtaining (Cangi et al., 2020) (where W is water):

$$W_{\text{lost}} = W_{\text{now}} \left(\left(\frac{(\text{D}/\text{H})_{\text{now}}}{(\text{D}/\text{H})_{\text{past}}} \right)^{1/(1-f)} - 1 \right) \quad (6)$$

Implicit in these equations is the assumption that $[\text{H}] \gg [\text{D}]$, so that the past and present abundances of H_2O are reasonable representations of the entire water budget. In the present day, the ratio of D/H is well constrained by many observational studies to be approximately $4-6 \times$ standard mean ocean water (SMOW) (Encrenaz et al., 2018; Villanueva et al., 2015, and references therein). Current research also has identified a likely present-day exchangeable reservoir water budget of 20-30 m GEL (Lasue et al., 2013, and references therein). By obtaining a reliable value for f , we can combine all these values to calculate the inventory of water on ancient Mars.

Cangi et al. (2020) suggested that the difference between the mean atmospheric f_t (considering only thermal escape) and f_{tn} (considering both thermal and non-thermal escape)

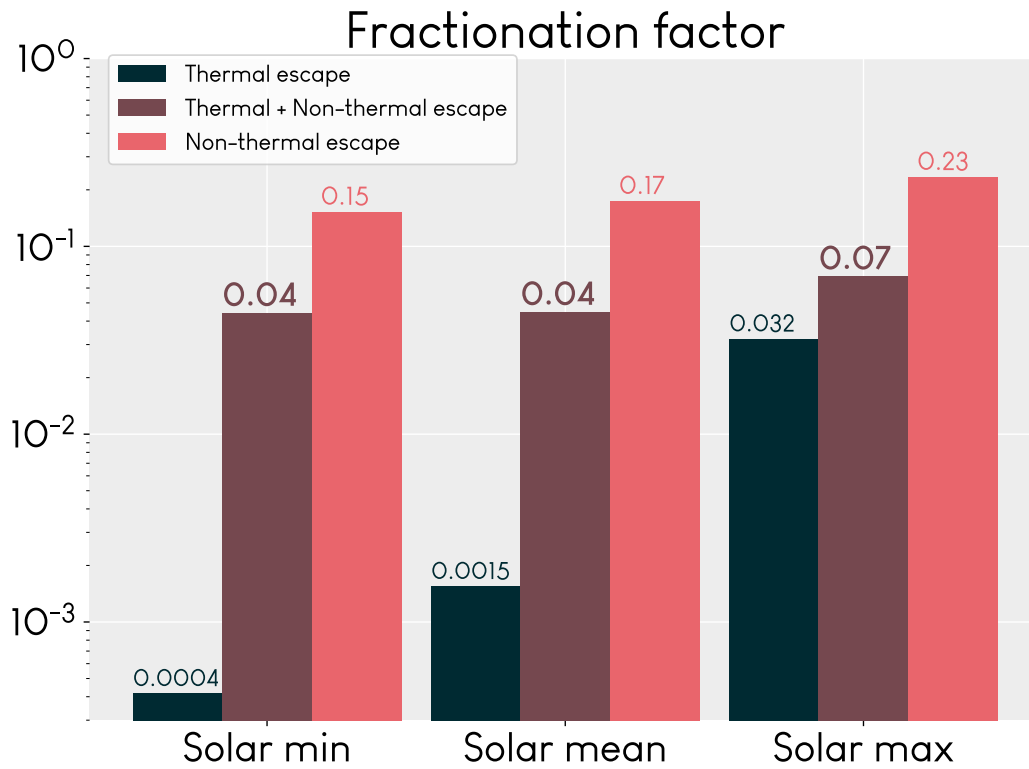


Figure 8. The fractionation factor f for three different modes of escape. Increased solar activity leads to a moderate increase in total f , and inclusion of non-thermal escape increases total f by 1-2 orders of magnitude during solar minimum and mean. Fractionation represents the escape efficiency of D compared to H, meaning that $f = 0.04$ represents a 4% escape efficiency of D. Non-thermal escape is an effective escape method for D under all solar conditions.

was several orders of magnitude. Because they did not directly model non-thermal escape, they arrived at this conclusion by incorporating the non-thermal escape velocity given by V. A. Krasnopolsky et al. (1998) into their model. We are now in a position to compare with those estimates; our calculations of the fractionation factor are shown in Figure 8. Cangi et al. (2020) calculated $f = 0.06$ for their standard atmosphere, based on their modeled thermal escape and estimated non-thermal escape. We calculate a total escape fractionation of $f = 0.04$ for our solar mean atmosphere, which has the same insolation and similar temperatures, and is not far off from their 0.06. Our results are consistent with their thermal escape $f = 0.002$ for the standard atmosphere (roughly equivalent to our solar mean atmosphere). Our results show that while overall D escape at Mars is around 4-7% as efficient as H escape, non-thermal D escape is much more efficient, between 15-23% that of H.

Our results yield integrated water loss of 147–158 m GEL (present day exchangeable reservoir = 30 m GEL, $f = 0.04$ –0.07, D/H=5.5×SMOW). This total loss still does not agree with the geological estimates of 500+ m GEL (Lasue et al., 2013). The discrepancy is summarized in Figure 9. Figure 9a shows the gap between the amount of water loss calculated by atmospheric models (Yung et al., 1988; Kass & Yung, 1999; V. Krasnopolsky, 2000; V. A. Krasnopolsky, 2002; Cangi et al., 2020) and that inferred from geomorphological observations (Lasue et al., 2013, and references therein). The time-averaged H escape rate curve suggests that the rates observed today (Jakosky et al., 2018) are unlikely to be near the average, and that escape was likely higher in the distant past, enabling greater water loss. Plausible explanations could include periods of hydrodynamic escape, a more EUV-active young sun driving greater photochemistry, extreme obliquities (Wordsworth, 2016; Laskar et al., 2004), or other as of yet unknown dynamics.

It is also possible that some water may have been sequestered into the surface. Recent work by Scheller et al. (2021) suggests that this amount may have accounted for between 30-99% of all missing water. More smaller-scale models and many observations will be needed to constrain this large range further. Hydrated minerals may contain 130-260 m GEL equivalent water Wernicke and Jakosky (2021), but the time of emplacement and any fractionation of the process is unclear. In general, due to the chaotic evolution of obliquity (Laskar et al., 2004) over Mars’ history, it is extremely difficult to qualitatively describe escape rates in the past. Although it is difficult to extrapolate much from the present-day rates, high loss of water via escape to space is not ruled out.

Figure 9b also helps demonstrate when it is important to know the value of f rather precisely. Discriminating between $f = 0.04$ or $f = 0.07$ is not particularly important: below $f = 0.1$, water loss curves are relatively vertical, meaning that a change in f does not equate to a significant change in water loss, but this is less true the closer f gets to 1. (For another view, see Figure S4 for water loss as a function of f for a single D/H ratio.)

Considered together, these insights tell us that non-thermal escape processes for D are important to model in order to accurately understand how D escapes from Mars. This conclusion may not hold for other planets, moons, or exoplanets; on bodies which are colder, larger, or otherwise less conducive to thermal escape, non-thermal escape may have a greater role to play.

4.2 Other non-thermal processes

As mentioned earlier, we do not model interactions with the solar wind. Lewkow and Kharchenko (2014) have calculated that penetrating solar wind protons can produce $4.18 \times 10^4 \text{ cm}^{-2}\text{s}^{-1}$ energetic neutral H atoms (ENAs) which escape. This is a negligible amount compared to our total non-thermal H escape, which is $6.5 \times 10^7 \text{ cm}^{-2}\text{s}^{-1}$, so we do not expect it to change our results. Without a value for D ENAs, we cannot make an immediate comparison, but we can calculate what fraction of our total H column the H ENAs

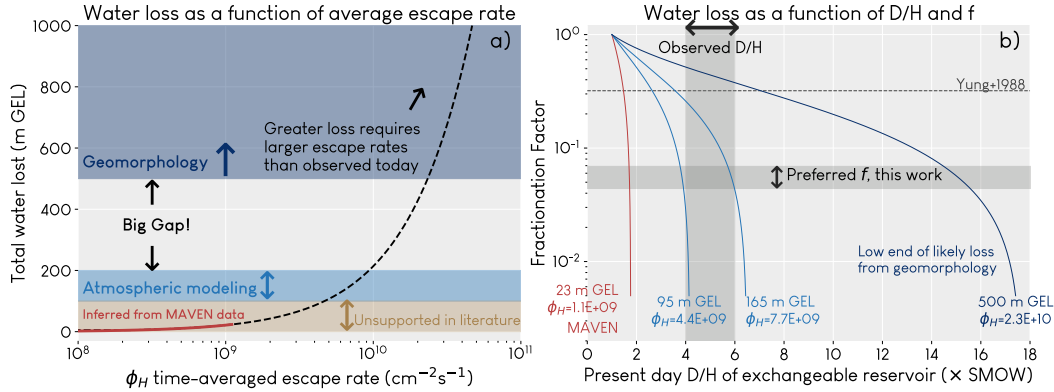


Figure 9. a): Possible water loss as a function of long-term average H escape rate ϕ_H , $W_{\text{lost}} = \bar{\phi}_H t$, where $t = 4.5$ billion years. A significant gap separates the amount of water loss inferred from atmospheric modeling and geomorphological studies. Additionally, escape rates determined from MAVEN data enable very small amounts of water loss that are not consistent with the geological evidence. b): Water loss lines represent solutions to equation 6, assuming 30 m GEL in the present-day exchangeable reservoir. The regions matching the best values of D/H and f are shaded in gray, with the overlapped rectangle representing our best estimate of the present-day atmosphere. (The fractionation factor calculated by Yung et al. (1988) is shown for reference, though it is high due to the highly uncertain exospheric temperatures then used.)

make up. For our solar mean model (Figure S1), the fraction is 8×10^{-11} . If we multiply this fraction by our D column, we obtain an additional $25 \text{ cm}^{-2}\text{s}^{-1}$ non-thermally escaping D atoms. Solar wind penetration should thus be negligible for the non-thermal escape we calculate at the altitudes we model, but an important interaction to consider during times of extreme solar activity or at higher altitudes in the exosphere. A future study on D ENA production would also help refine this contribution's value.

We do not account for the collision of hydrogen atoms or molecules with hot oxygen, which is another significant source of hot atoms in the martian atmosphere. Assuming an exospheric temperature of 240 K, Gacesa et al. (2012) calculated that $1.9 \times 10^5 \text{ cm}^{-2}\text{s}^{-1}$ H_2 molecules escape as a result of collision with hot oxygen, which is larger than our non-thermal H_2 flux by 1-2 orders of magnitude depending on solar conditions (see Table 2). They also estimate that $74 \text{ HD molecules cm}^{-2}\text{s}^{-1}$ escape via this mechanism. This would bring our total HD escape to approximately $100 \text{ cm}^{-2}\text{s}^{-1}$, an order of magnitude larger than our current result. Other species may also play a role; Gacesa et al. (2017) calculate that the total non-thermal escape of OH is $1.07 \times 10^{23} \text{ s}^{-1}$, i.e. $7.4 \times 10^5 \text{ cm}^{-2}\text{s}^{-1}$. Even added together, these numbers are all still orders of magnitude smaller than the non-thermal atomic escape fluxes, and will not significantly affect our results. If we included them, the net effect would be to boost H escape, decreasing the fractionation factor and total water loss.

Energization of atomic H and D by collision with hot oxygen may be more significant. Shematovich (2013) estimates, for specific density profiles and temperatures, a total possible escape flux of hot H produced this way to be $6 \times 10^6 \text{ cm}^{-2}\text{s}^{-1}$ at low solar activity. This is 9% of our non-thermal H escape (see Table 2). Our non-thermal D escape is 3 orders of magnitude lower than the H escape. If we apply this scaling relation to hot O collisions with D, we can expect that this pathway might produce D escape on the order of 10^3 , which is the same order as our calculated non-thermal escape fluxes. If we instead generously assumed an extra 9×10^3 hot D atoms produced from collision with

hot O, doubling our total, we would expect to also double our fractionation factor, to $f = 0.08 - 0.14$.

4.3 Future opportunities and directions

There are several things that could enhance our model. The first likely avenue worthy of exploration would be to perform a similar study, but with a more physically-motivated parameterization of atomic O escape. Fixing the O escape at $1.2 \times 10^8 \text{ cm}^{-2}\text{s}^{-1}$ was sufficient for the scope of this work; our results represent long-term equilibrium, when it is possible to adopt reasonable means for parameters like O escape. Adding a dynamically evolving escape flux boundary condition for atomic O would enable a more comprehensive understanding of shorter-term variations in H and D escape rates, such as a result of regular seasonal cycles. This would better capture the interplay between the hydrogen species and CO_2 , the main component of the atmosphere and a significant source of O. This would also present an opportunity to include processes more important to O loss, such as ion pickup, ion/polar outflow, and sputtering. We do not include these as we focus on H and D loss, which are dominated by other processes.

We have also been forced to make some unavoidable assumptions about the basic chemistry, owing to a lack of laboratory data. While we have made a best attempt to use existing reaction rate coefficient data from several different papers and databases, a comprehensive catalogue of rate coefficients, branching ratios, and cross sections for deuterated reactions is not available in the literature at this time. Most especially, future photochemical models would benefit from accurate photoabsorption cross sections for deuterated neutrals other than HDO (including OD and HD in particular), and measured reaction rate coefficients for as many of the deuterated reactions with estimated rates in Table 1 as possible. While not all reactions will significantly affect the chemistry, certain rates that dominate production or loss of a species can have strong effects, affecting densities up to a few orders of magnitude (see, for example, Fox et al. (2017)).

Photochemical modeling often entails excluding some important processes that are better captured in higher-dimensional models. Bluejay is the first photochemical model to couple the ion and neutral atmospheres from the upper atmosphere down to the surface, but there is still an opportunity for future work to give more attention to surface-atmosphere interactions. Our inclusion of surface-atmosphere interactions is primarily relegated to surface density boundary conditions for certain species. A more detailed parameterization of processes such as volcanic outgassing, major seasonal changes in the polar caps, water adsorption and desorption on dust grains and dust lifting, deposition of volatiles, and the role of non-volatiles such as perchlorates, salts, and other non-water ices could yield new insights into the planetary climate system as a whole.

Our results also have implications for the detectability of deuterated ions by present and future Mars missions. Using MAVEN’s NGIMS instrument, the deuterated ions that we model typically occupy the same mass/charge ratio bin as a more prevalent H-bearing species. For example, D^+ occupies the same bin as H_2^+ , but the latter is far more abundant. The deuterated species in our model which do not overlap with an H-bearing species are H_2D^+ (mass bin 4), HD_2^+ (5), H_2DO^+ (20), HDO_2^+ (35), and ArD^+ (42). However, several of these species are expected to be very rarefied and thus difficult to detect, and others may overlap with species we do not model that do exist on Mars, such as helium in mass bin 4. These degeneracies make obtaining deuterated ion densities challenging; doing so will require inventive methods applied to existing data or new methods with new instruments.

5 Conclusions

We have used a 1D photochemical model, bluejay, that fully couples ions and neutrals from surface to space to study production of hot D from planetary ionospheric processes. We show that the deuterated ionosphere behaves relatively similar to the H-bearing iono-

sphere. This result is somewhat expected, as measurements of rate coefficients for deuterated reactions are much less available than the H-bearing counterpart reaction rate coefficients.

For the first time, we have self-consistently quantified, in raw flux and in percent of total escape, the thermal and non-thermal escape fluxes of H, D, H₂, and HD sourced from planetary ionospheric reactions under different solar conditions. We also show the first identification of the dominant chemical reactions which produce hot D. Our results confirm earlier suggestions that non-thermal escape dominates D escape at Mars, although our results have shown that this is true throughout the solar cycle rather than just during quiet solar conditions.

We also confirm an earlier prediction (Cangi et al., 2020) that including non-thermal escape when calculating the D/H fractionation factor will result in a fractionation factor several orders of magnitude higher than if it is neglected. However, the resulting fractionation factor is 0.04–0.07, meaning that D escape is only about 4–7% as efficient as H escape. If the fractionation has consistently been this small, and we also assume that ϕ_H has been similar to the value today through time, it is difficult to ascribe the large amount of water loss that we see indicated in the rock record to atmospheric escape alone. On the other hand, the dust storm season on Mars, as well as normal seasonal variations between perihelion and aphelion, are characterized by spatially and temporally localized enhancements of the D/H ratio, water abundance, and H escape (Villanueva et al., 2022; Daerden et al., 2022; A. Fedorova et al., 2021; Chaffin et al., 2021; Holmes et al., 2021; A. A. Fedorova et al., 2020; Stone et al., 2020; Aoki et al., 2019; Vandaele et al., 2019; Heavens et al., 2018; Chaffin et al., 2017, and references therein). It is not yet clear if enhanced D escape or a heightened fractionation factor also occur along with these seasonal changes, although it seems likely (Alday et al., 2021); if they do, then the assumption of a constant fractionation factor over time cannot hold, and we will have to introduce some additional nuance to our use of Rayleigh fractionation to estimate water loss.

Ongoing improvements in modeling, especially coupling between 1D and 3D models, as well as continual advancements in instrumentation for planetary missions will be necessary to continue putting together the puzzle of water on Mars throughout history.

6 Open Research Statement

The photochemical model, bluejay, used for this work is written for and compatible with Julia 1.8.5 (Bezanson et al., 2017). The model itself, in version 1.0 as used in this work, is available at Zenodo (Cangi & Chaffin, 2022).

A typical use-case of the model is to modify simulation parameters within `PARAMETERS.jl` and to then call `julia converge_new_file.jl` at the command line.

Acknowledgments

This work was supported by three separate funding sources. First, this work was supported by Mars Data Analysis Program grant #NNX14AM20G. Second, this material is based upon work supported by the National Science Foundation Graduate Research Fellowship Program under Grant No. DGE 1650115. Any opinions, findings, and conclusions or recommendations expressed in this material are those of the author(s) and do not necessarily reflect the views of the National Science Foundation. Third, this work was supported by NASA’s FINESST Program (Grant #80NSSC22K1326).

References

Alday, J., Trokhimovskiy, A., Irwin, P. G. J., Wilson, C. F., Montmessin, F., Lefèvre, F., . . . Shakun, A. (2021, June). Isotopic fractionation of water

- and its photolytic products in the atmosphere of Mars. *Nature Astronomy*, *5*, 943-950. doi: 10.1038/s41550-021-01389-x
- AlMaazmi, H., Chaffin, M., Forget, F., Millour, E., & Deighan, J. (2019, July). C-Storm Effect on the Escape of Hydrogen in the Martian Atmosphere Using the LMD-GCM. In LPI Editorial Board (Ed.), *Ninth international conference on mars* (Vol. 2089, p. 6208).
- Alsaeed, N. R., & Jakosky, B. M. (2019). Mars Water and D/H Evolution From 3.3 Ga to Present. *Journal of Geophysical Research: Planets*, *124*. doi: 10.1029/2019JE006066
- Anicich, V. G. (1993, November). Evaluated Bimolecular Ion-Molecule Gas Phase Kinetics of Positive Ions for Use in Modeling Planetary Atmospheres, Cometary Comae, and Interstellar Clouds. *Journal of Physical and Chemical Reference Data*, *22*(6), 1469-1569. doi: 10.1063/1.555940
- Anicich, V. G. (2003). *An index of the literature for bimolecular gas phase cation-molecule reaction kinetics* (JPL Publication No. 03-19). Pasadena: Jet Propulsion Laboratory.
- Aoki, S., Vandaele, A. C., Daerden, F., Villanueva, G. L., Liuzzi, G., Thomas, I. R., ... Lopez-Moreno, J. J. (2019). Water Vapor Vertical Profiles on Mars in Dust Storms Observed by TGO/NOMAD. *Journal of Geophysical Research (Planets)*, *124*(12), 3482-3497. doi: 10.1029/2019JE006109
- Atkinson, R., Baulch, D. L., Cox, R. A., Hampson, R. F., Kerr Chairman, J. A., & Troe, J. (1989, April). Evaluated Kinetic and Photochemical Data for Atmospheric Chemistry: Supplement III. IUPAC Subcommittee on Gas Kinetic Data Evaluation for Atmospheric Chemistry. *Journal of Physical and Chemical Reference Data*, *18*(2), 881-1097. doi: 10.1063/1.555832
- Banaszkiewicz, M., Lara, L. M., Rodrigo, R., López-Moreno, J. J., & Molina-Cuberos, G. J. (2000, October). A Coupled Model of Titan's Atmosphere and Ionosphere. *Icarus*, *147*(2), 386-404. doi: 10.1006/icar.2000.6448
- Bauer, S. J. (1973). Chemical processes. In *Physics of planetary ionospheres* (pp. 82-95). Springer.
- Baulch, D. L., Bowman, C. T., Cobos, C. J., Cox, R. A., Just, T., Kerr, J. A., ... Warnatz, J. (2005, September). Evaluated Kinetic Data for Combustion Modeling: Supplement II. *Journal of Physical and Chemical Reference Data*, *34*(3), 757-1397. doi: 10.1063/1.1748524
- Baulch, D. L., Cobos, C. J., Cox, R. A., Esser, C., Frank, P., Just, T., ... Warnatz, J. (1992, May). Evaluated Kinetic Data for Combustion Modelling. *Journal of Physical and Chemical Reference Data*, *21*(3), 411-734. doi: 10.1063/1.555908
- Benna, M., Mahaffy, P. R., Grebowsky, J. M., Fox, J. L., Yelle, R. V., & Jakosky, B. M. (2015, November). First measurements of composition and dynamics of the Martian ionosphere by MAVEN's Neutral Gas and Ion Mass Spectrometer. *Geophysical Research Letters*, *42*(21), 8958-8965. doi: 10.1002/2015GL066146
- Bertaux, J.-L., & Montmessin, F. (2001, December). Isotopic fractionation through water vapor condensation: The Deuteropause, a cold trap for deuterium in the atmosphere of Mars. *J. Geophys. Res.*, *106*(E12), 32879-32884. doi: 10.1029/2000JE001358
- Bezanson, J., Edelman, A., Karpinski, S., & Shah, V. B. (2017). Julia: A fresh approach to numerical computing. *SIAM review*, *59*(1), 65-98.
- Bhattacharyya, D., Chaufray, J. Y., Mayyasi, M., Clarke, J. T., Stone, S., Yelle, R. V., ... Schneider, N. M. (2020). Two-dimensional model for the martian exosphere: Applications to hydrogen and deuterium Lyman α observations. *Icarus*, *339*, 113573. doi: 10.1016/j.icarus.2019.113573
- Bhattacharyya, D., Clarke, J. T., Chaufray, J. Y., Mayyasi, M., Bertaux, J. L., Chaffin, M. S., ... Villanueva, G. L. (2017). Seasonal Changes in Hydrogen Escape From Mars Through Analysis of HST Observations of the Martian Exosphere Near Perihelion. *Journal of Geophysical Research (Space Physics)*,

- 122(11), 11,756-11,764. doi: 10.1002/2017JA024572
- Borodi, G., Luca, A., & Gerlich, D. (2009, February). Reactions of CO₂⁺ with H, H₂ and deuterated analogues. *International Journal of Mass Spectrometry*, 280(1-3), 218-225. doi: 10.1016/j.ijms.2008.09.004
- Brain, D. A., McFadden, J. P., Halekas, J. S., Connerney, J. E. P., Bougher, S. W., Curry, S., . . . Seki, K. (2015, November). The spatial distribution of planetary ion fluxes near Mars observed by MAVEN. *Geophys. Res. Lett.*, 42(21), 9142-9148. doi: 10.1002/2015GL065293
- Brian, J., & Mitchell, A. (1990). The dissociative recombination of molecular ions. *Physics Reports*, 186(5), 215-248.
- Brune, W. H., Schwab, J. J., & Anderson, J. (1983). Laser magnetic resonance, resonance fluorescence, resonance absorption studies of the reaction kinetics of atomic oxygen+ hydroxyl. fwardw. atomic hydrogen+ molecular oxygen, atomic oxygen+ perhydroxyl. fwardw. hydroxyl+ molecular oxygen, atomic nitrogen+ hydroxyl. fwardw. atomic hydrogen+ nitric oxide, atomic nitrogen+ perhydroxyl. fwardw. products at 300 k between 1 and 5 torr. *The Journal of Physical Chemistry*, 87(22), 4503-4514.
- Burkholder, J., Sander, S., Abbatt, J., Barker, J., Cappa, C., Crouse, J., . . . Wine, P. H. (2019). *Chemical kinetics and photochemical data for use in atmospheric studies, evaluation no. 19* (JPL Publication No. Publication 19-5). Pasadena: Jet Propulsion Laboratory.
- Burkholder, J. B., Sander, S. P., Abbatt, J., Barker, J. R., Huie, R., Kolb, C., . . . Wine, P. (2015). *Chemical kinetics and photochemical data for use in atmospheric studies: evaluation number 18* (JPL Publication No. Publication 15-10). Pasadena: Jet Propulsion Laboratory.
- Campbell, I. M., & Gray, C. N. (1973, February). Rate constants for O(³P) recombination and association with N(⁴S). *Chemical Physics Letters*, 18(4), 607-609. doi: 10.1016/0009-2614(73)80479-8
- Cangi, E. M., & Chaffin, M. (2022, December). *bluejay: Atmospheric photochemistry in julia*. Zenodo. Retrieved from <https://doi.org/10.5281/zenodo.7735302> doi: 10.5281/zenodo.7735302
- Cangi, E. M., Chaffin, M. S., & Deighan, J. (2020). Higher Martian Atmospheric Temperatures at All Altitudes Increase the D/H Fractionation Factor and Water Loss. *Journal of Geophysical Research: Planets*, 125(12), 1-15. doi: 10.1029/2020JE006626
- Cassata, W. S., Zahnle, K. J., Samperton, K. M., Stephenson, P. C., & Wimpenny, J. (2022, February). Xenon isotope constraints on ancient Martian atmospheric escape. *Earth and Planetary Science Letters*, 580, 117349. doi: 10.1016/j.epsl.2021.117349
- Cazaux, S., Cobut, V., Marseille, M., Spaans, M., & Caselli, P. (2010, November). Water formation on bare grains: When the chemistry on dust impacts interstellar gas. *Astronomy & Astrophysics*, 522, A74. doi: 10.1051/0004-6361/201014026
- Chaffin, M. S., Chaufray, J. Y., Deighan, J., Schneider, N. M., Mayyasi, M., Clarke, J. T., . . . Jakosky, B. M. (2018, August). Mars H Escape Rates Derived From MAVEN/IUVS Lyman Alpha Brightness Measurements and Their Dependence on Model Assumptions. *Journal of Geophysical Research (Planets)*, 123(8), 2192-2210. doi: 10.1029/2018JE005574
- Chaffin, M. S., Deighan, J., Schneider, N. M., & Stewart, A. I. F. (2017, January). Elevated atmospheric escape of atomic hydrogen from Mars induced by high-altitude water. *Nature Geoscience*, 10(3), 174-178. doi: 10.1038/ngeo2887
- Chaffin, M. S., Kass, D. M., Aoki, S., Fedorova, A. A., Deighan, J., Connour, K., . . . Korablev, O. I. (2021, August). Martian water loss to space enhanced by regional dust storms. *Nature Astronomy*, 5, 1036-1042. doi: 10.1038/s41550-021-01425-w

- Chamberlain, J. W., & Hunten, D. M. (1987). *Theory of planetary atmospheres. An introduction to their physics and chemistry*. (Vol. 36).
- Chaufray, J. Y., Gonzalez-Galindo, F., Lopez-Valverde, M. A., Forget, F., Quémerais, E., Bertaux, J. L., ... Yelle, R. V. (2021, January). Study of the hydrogen escape rate at Mars during martian years 28 and 29 from comparisons between SPICAM/Mars express observations and GCM-LMD simulations. *Icarus*, *353*, 113498. doi: 10.1016/j.icarus.2019.113498
- Chaufray, J. Y., Mayyasi, M., Chaffin, M., Deighan, J., Bhattacharyya, D., Clarke, J., ... Jakosky, B. (2021, April). Estimate of the D/H Ratio in the Martian Upper Atmosphere from the Low Spectral Resolution Mode of MAVEN/IUVS. *Journal of Geophysical Research (Planets)*, *126*(4), e06814. doi: 10.1029/2020JE006814
- Cheng, B.-M., Chew, E. P., Liu, C.-P., Bahou, M., Lee, Y.-P., Yung, Y. L., & Gerstell, M. F. (1999, December). Photo-induced fractionation of water isotopomers in the Martian atmosphere. *Geophys. Res. Lett.*, *26*(24), 3657-3660. doi: 10.1029/1999GL008367
- Cheng, B. M., Chung, C. Y., Bahou, M., Lee, Y. P., Lee, L. C., Van Harreveld, R., & Van Hemert, M. C. (2004). Quantitative spectroscopic and theoretical study of the optical absorption spectra of H₂O, HOD, and D₂O in the 125-145 nm region. *Journal of Chemical Physics*, *120*(1), 224-229. doi: 10.1063/1.1630304
- Daerden, F., Neary, L., Villanueva, G., Liuzzi, G., Aoki, S., Clancy, R. T., ... Vandaele, A. C. (2022, February). Explaining NOMAD D/H Observations by Cloud-Induced Fractionation of Water Vapor on Mars. *Journal of Geophysical Research (Planets)*, *127*(2), e07079. doi: 10.1029/2021JE007079
- Davidson, J. A., Schiff, H. I., Brown, T. J., & Howard, C. J. (1978, August). Temperature dependence of the deactivation of O(¹D) by CO from 113-333 K. *J. Chem. Phys.*, *69*(3), 1216-1217. doi: 10.1063/1.436657
- Deighan, J. (2012). *The effect of an ozone layer on ancient mars* (Doctoral dissertation, University of Virginia). Retrieved from <http://libra.virginia.edu/catalog/libra-oa:2577>
- Dobrijevic, M., Loison, J. C., Hickson, K. M., & Gronoff, G. (2016, April). 1D-coupled photochemical model of neutrals, cations and anions in the atmosphere of Titan. *Icarus*, *268*, 313-339. doi: 10.1016/j.icarus.2015.12.045
- Dong, Y., Fang, X., Brain, D. A., McFadden, J. P., Halekas, J. S., Connerney, J. E., ... Jakosky, B. M. (2015, November). Strong plume fluxes at Mars observed by MAVEN: An important planetary ion escape channel. *Geophys. Res. Lett.*, *42*(21), 8942-8950. doi: 10.1002/2015GL065346
- Doroshenko, V., Kudryavtsev, N., & Smetanin, V. (1992). Quenching mechanisms for electronically excited species in partially dissociated air. *HIGH ENERGY CHEMISTRY*, *26*(4), 227-230.
- Dutuit, O., Carrasco, N., Thissen, R., Vuitton, V., Alcaraz, C., Pernot, P., ... Lavvas, P. (2013, February). Critical Review of N, N⁺, N⁺², N⁺⁺, and N⁺⁺² Main Production Processes and Reactions of Relevance to Titan's Atmosphere. *ApJS*, *204*(2), 20. doi: 10.1088/0067-0049/204/2/20
- Encrenaz, T., DeWitt, C., Richter, M. J., Greathouse, T. K., Fouchet, T., Montmessin, F., ... Sagawa, H. (2018, April). New measurements of D/H on Mars using EXES aboard SOFIA. *Astronomy & Astrophysics*, *612*, A112. doi: 10.1051/0004-6361/201732367
- Ergun, R. E., Morooka, M. W., Andersson, L. A., Fowler, C. M., Delory, G. T., Andrews, D. J., ... Jakosky, B. M. (2015, November). Dayside electron temperature and density profiles at Mars: First results from the MAVEN Langmuir probe and waves instrument. *Geophysical Research Letters*, *42*(21), 8846-8853. doi: 10.1002/2015GL065280
- Fedorova, A., Montmessin, F., Korablev, O., Lefèvre, F., Trokhimovskiy, A., & Bertaux, J.-L. (2021, January). Multi-Annual Monitoring of the Water Va-

- por Vertical Distribution on Mars by SPICAM on Mars Express. *Journal of Geophysical Research (Planets)*, 126(1), e06616. doi: 10.1029/2020JE006616
- Fedorova, A. A., Montmessin, F., Korablev, O., Luginin, M., Trokhimovskiy, A., Belyaev, D. A., . . . Wilson, C. F. (2020, January). Stormy water on Mars: The distribution and saturation of atmospheric water during the dusty season. *Science*, 367(6475), 297-300. doi: 10.1126/science.aay9522
- Fehsenfeld, F. C., Dunkin, D. B., & Ferguson, E. E. (1970, August). Rate constants for the reaction of CO_2^+ with O, O_2 and NO; N_2^+ with O and NO; and O_2^+ with NO. *Planetary and Space Science*, 18(8), 1267-1269. doi: 10.1016/0032-0633(70)90216-3
- Fletcher, I., & Husain, D. (1976). The collisional quenching of electronically excited oxygen atoms, $\text{O}(^1\text{D})$, by the gases NH_3 , H_2O , C_2H_6 , C_3H_8 , and $\text{C}(\text{CH}_3)_4$, using time-resolved attenuation of atomic resonance radiation. *Canadian Journal of Chemistry*, 54(11), 1765-1770.
- Fox, J. L. (1993, February). The production and escape of nitrogen atoms on Mars. *J. Geophys. Res.*, 98(E2), 3297-3310. doi: 10.1029/92JE02289
- Fox, J. L. (2015, May). The chemistry of protonated species in the martian ionosphere. *Icarus*, 252, 366-392. doi: 10.1016/j.icarus.2015.01.010
- Fox, J. L., Benna, M., Mahaffy, P. R., & Jakosky, B. M. (2015, November). Water and water ions in the Martian thermosphere/ionosphere. *Geophysical Research Letters*, 42(21), 8977-8985. doi: 10.1002/2015GL065465
- Fox, J. L., Benna, M., McFadden, J. P., Jakosky, B. M., & MAVEN NGIMS Team. (2021, April). Rate coefficients for the reactions of CO_2^+ with O: Lessons from MAVEN at Mars. *Icarus*, 358, 114186. doi: 10.1016/j.icarus.2020.114186
- Fox, J. L., & Hać, A. B. (2009, December). Photochemical escape of oxygen from Mars: A comparison of the exobase approximation to a Monte Carlo method. *Icarus*, 204(2), 527-544. doi: 10.1016/j.icarus.2009.07.005
- Fox, J. L., Johnson, A. S., Ard, S. G., Shuman, N. S., & Viggiano, A. A. (2017, August). Photochemical determination of O densities in the Martian thermosphere: Effect of a revised rate coefficient. *Geophysical Research Letters*, 44(16), 8099-8106. doi: 10.1002/2017GL074562
- Gacesa, M., Lewkow, N., & Kharchenko, V. (2017). Non-thermal production and escape of OH from the upper atmosphere of Mars. *Icarus*, 284, 90-96.
- Gacesa, M., Lillis, R., Deighan, J., Elrod, M., Fox, J. L., & the MAVEN NGIMS team. (2018). Non-thermal escape rates of light species from Mars using MAVEN in-situ measurements. In *European planetary science congress* (pp. EPSC2018-604).
- Gacesa, M., Zhang, P., & Kharchenko, V. (2012, May). Non-thermal escape of molecular hydrogen from Mars. *Geophysical Research Letters*, 39(10), L10203. doi: 10.1029/2012GL050904
- Geppert, W. D., Reignier, D., Stoecklin, T., Naulin, C., Costes, M., Chastaing, D., . . . Smith, I. W. M. (2000, January). Comparison of the cross-sections and thermal rate constants for the reactions of $\text{C}(^3\text{P})$ atoms with O_2 and NO. *Physical Chemistry Chemical Physics (Incorporating Faraday Transactions)*, 2(13), 2873-2881. doi: 10.1039/B002583F
- Geppert, W. D., Thomas, R., Ehlerding, A., Semaniak, J., Österdahl, F., Af Ugglas, M., . . . Larsson, M. (2004, January). Extraordinary branching ratios in astrophysically important dissociative recombination reactions. *Faraday Discussions*, 127, 425. doi: 10.1039/b314005a
- Geppert, W. D., Thomas, R. D., Ehlerding, A., Hellberg, F., Österdahl, F., Hamberg, M., . . . Larsson, M. (2005, January). Dissociative recombination branching ratios and their influence on interstellar clouds. In *Journal of physics conference series* (Vol. 4, p. 26-31). doi: 10.1088/1742-6596/4/1/004
- Gregory, B. S., Chaffin, M. S., Elliott, R. D., Deighan, J., Gröller, H., & Cangi, E. M. (2023). Nonthermal hydrogen loss at Mars: Contributions of photo-

- chemical mechanisms to escape and identification of key processes. *Journal of Geophysical Research (Planets)*, tbd(tbd). doi: tbd
- Gregory, B. S., Elliott, R. D., Deighan, J., Gröller, H., & Chaffin, M. S. (2023, January). HCO⁺ Dissociative Recombination: A Significant Driver of Nonthermal Hydrogen Loss at Mars. *Journal of Geophysical Research (Planets)*, 128(1), e2022JE007576. doi: 10.1029/2022JE007576
- Gu, H., Cui, J., Huang, X., & Sun, M. (2022, May). Wind-Enhanced Hydrogen Escape on Mars. *Geophys. Res. Lett.*, 49(10), e98312. doi: 10.1029/2022GL098312
- Gustafsson, M., & Nyman, G. (2015, April). Radiative association rate constant for the formation of CO: the importance of the first excited ¹Σ⁺ state. *MNRAS*, 448(3), 2562-2565. doi: 10.1093/mnras/stv089
- Halekas, J. S. (2017, May). Seasonal variability of the hydrogen exosphere of Mars. *Journal of Geophysical Research (Planets)*, 122(5), 901-911. doi: 10.1002/2017JE005306
- Halekas, J. S., Brain, D. A., Luhmann, J. G., DiBraccio, G. A., Ruhunusiri, S., Harada, Y., ... Jakosky, B. M. (2017, November). Flows, Fields, and Forces in the Mars-Solar Wind Interaction. *Journal of Geophysical Research (Space Physics)*, 122(11), 11,320-11,341. doi: 10.1002/2017JA024772
- Hanley, K. G., Fowler, C. M., McFadden, J. P., Mitchell, D. L., & Curry, S. (2022, September). MAVEN-STATIC Observations of Ion Temperature and Initial Ion Acceleration in the Martian Ionosphere. *Geophys. Res. Lett.*, 49(18), e2022GL100182. doi: 10.1029/2022GL100182
- Heavens, N. G., Kleinböhl, A., Chaffin, M. S., Halekas, J. S., Kass, D. M., Hayne, P. O., ... Schofield, J. T. (2018). Hydrogen escape from Mars enhanced by deep convection in dust storms. *Nature Astronomy*, 2(2), 126-132. doi: 10.1038/s41550-017-0353-4
- Herd, C. R., Adams, N. G., & Smith, D. (1990, January). OH Production in the Dissociative Recombination of H₂O⁺, HCO⁺, and N₂O⁺: Comparison with Theory and Interstellar Implications. *ApJ*, 349, 388. doi: 10.1086/168322
- Herron, J. T. (1999, September). Evaluated Chemical Kinetics Data for Reactions of N₂(²D) N(²P), and N₂(A³Σ⁺_u) in the Gas Phase. *Journal of Physical and Chemical Reference Data*, 28(5), 1453-1483. doi: 10.1063/1.556043
- Hierl, P. M., Morris, R. A., & Viggiano, A. A. (1997, June). Rate coefficients for the endothermic reactions C⁺(²P) + H₂(D₂) → CH⁺(CD⁺) + H(D) as functions of temperature from 400-1300 K. *J. Chem. Phys.*, 106(24), 10145-10152. doi: 10.1063/1.474093
- Holmes, J. A., Lewis, S. R., Patel, M. R., Chaffin, M. S., Cangi, E. M., Deighan, J., ... Vandaale, A. C. (2021, October). Enhanced water loss from the martian atmosphere during a regional-scale dust storm and implications for long-term water loss. *Earth and Planetary Science Letters*, 571, 117109. doi: 10.1016/j.epsl.2021.117109
- Huebner, W., & Mukherjee, J. (2015). *Photo Ionization/Dissociation Rates*. Retrieved from <https://phidrates.space.swri.edu>
- Hunten, D. M., Pepin, R. O., & Walker, J. C. G. (1987, March). Mass fractionation in hydrodynamic escape. *Icarus*, 69(3), 532-549. doi: 10.1016/0019-1035(87)90022-4
- Jakosky, B. M., Brain, D., Chaffin, M., Curry, S., Deighan, J., Grebowsky, J., ... Zurek, R. (2018, November). Loss of the Martian atmosphere to space: Present-day loss rates determined from MAVEN observations and integrated loss through time. *Icarus*, 315, 146-157. doi: 10.1016/j.icarus.2018.05.030
- Jensen, M. J., Bilodeau, R. C., Heber, O., Pedersen, H. B., Safvan, C. P., Urbain, X., ... Andersen, L. H. (1999, October). Dissociative recombination and excitation of $\{\mathrm{H}\}_{-2}\{\mathrm{O}\}^{\{+}\}$ and

- $\{\mathrm{HDO}\}^+$. *Physical Review A*, 60(4), 2970–2976. Retrieved 2023-03-11, from <https://link.aps.org/doi/10.1103/PhysRevA.60.2970> (Publisher: American Physical Society) doi: 10.1103/PhysRevA.60.2970
- Jensen, M. J., Bilodeau, R. C., Safvan, C. P., Seiersen, K., Andersen, L. H., Pedersen, H. B., & Heber, O. (2000, November). Dissociative Recombination of $\mathrm{H}_3\mathrm{O}^+$, $\mathrm{HD}_2\mathrm{O}^+$, and $\mathrm{D}_3\mathrm{O}^+$. *ApJ*, 543(2), 764–774. doi: 10.1086/317137
- Kass, D. M., & Yung, Y. L. (1999, January). Water on Mars: Isotopic constraints on exchange between the atmosphere and surface. *Geophysical Research Letters*, 26(24), 3653–3656. doi: 10.1029/1999GL008372
- Kim, J., Nagy, A. F., Fox, J. L., & Cravens, T. E. (1998, December). Solar cycle variability of hot oxygen atoms at Mars. *J. Geophys. Res.*, 103(A12), 29339–29342. doi: 10.1029/98JA02727
- Klippenstein, S. J., Georgievskii, Y., & McCall, B. J. (2010, January). Temperature Dependence of Two Key Interstellar Reactions of H_3^+ : $\mathrm{O}(3\mathrm{P}) + \mathrm{H}_3^+$ and $\mathrm{CO} + \mathrm{H}_3^+$. *Journal of Physical Chemistry A*, 114(1), 278–290. doi: 10.1021/jp908500h
- Korolov, I., Plasil, R., Kotrik, T., Dohnal, P., & Glosik, J. (2009, February). Recombination of HCO^+ and DCO^+ ions with electrons. *International Journal of Mass Spectrometry*, 280(1–3), 144–148. doi: 10.1016/j.ijms.2008.07.023
- Krasnopolsky, V. (2000, December). NOTE: On the Deuterium Abundance on Mars and Some Related Problems. *Icarus*, 148(2), 597–602. doi: 10.1006/icar.2000.6534
- Krasnopolsky, V. A. (2002, December). Mars’ upper atmosphere and ionosphere at low, medium, and high solar activities: Implications for evolution of water. *Journal of Geophysical Research (Planets)*, 107(E12), 5128. doi: 10.1029/2001JE001809
- Krasnopolsky, V. A. (2010, June). Solar activity variations of thermospheric temperatures on Mars and a problem of CO in the lower atmosphere. *Icarus*, 207(2), 638–647. doi: 10.1016/j.icarus.2009.12.036
- Krasnopolsky, V. A. (2019, March). Photochemistry of water in the martian thermosphere and its effect on hydrogen escape. *Icarus*, 321, 62–70. doi: 10.1016/j.icarus.2018.10.033
- Krasnopolsky, V. A., Mumma, M. J., & Randall Gladstone, G. (1998, June). Detection of Atomic Deuterium in the Upper Atmosphere of Mars. *Science*, 280, 1576. doi: 10.1126/science.280.5369.1576
- Lammer, H., Kolb, C., Penz, T., Amerstorfer, U., Biernat, H., & Bodiselitsch, B. (2003). Estimation of the past and present martian water-ice reservoirs by isotopic constraints on exchange between the atmosphere and the surface. *International Journal of Astrobiology*, 2(3), 195–202.
- Larsson, M., Lepp, S., Dalgarno, A., Stroemholm, C., Sundstroem, G., Zengin, V., ... Datz, S. (1996, May). Dissociative recombination of $\mathrm{H}_2\mathrm{d}^+$ and the cosmic abundance of deuterium. *Astronomy and Astrophysics*, v.309, p.L1–L3, 309, L1. Retrieved 2023-03-11, from <https://ui.adsabs.harvard.edu/abs/1996A%26A...309L...1L/abstract>
- Laskar, J., Correia, A., Gastineau, M., Joutel, F., Levrard, B., & Robutel, P. (2004). Long term evolution and chaotic diffusion of the insolation quantities of Mars. *Icarus*, 170(2), 343–364. doi: 10.1016/J.ICARUS.2004.04.005
- Lasue, J., Mangold, N., Hauber, E., Clifford, S., Feldman, W., Gasnault, O., ... Mousis, O. (2013). Quantitative Assessments of the Martian Hydrosphere. *Space Science Reviews*, 174, 155–212. doi: 10.1007/s11214-012-9946-5
- Le Garrec, J. L., Carles, S., Speck, T., Mitchell, J. B. A., Rowe, B. R., & Ferguson, E. E. (2003, April). The ion-molecule reaction of O^+ with N_2 measured down to 23 K. *Chemical Physics Letters*, 372(3), 485–488. doi: 10.1016/S0009-2614(03)00377-4
- Leblanc, F., Modolo, R., Curry, S., Luhmann, J., Lillis, R., Chaufray, J. Y., ...

- Jakosky, B. (2015). Mars heavy ion precipitating flux as measured by Mars atmosphere and volatile evolution. *Geophysical Research Letters*, *42*(21), 9135-9141. Retrieved from <https://agupubs.onlinelibrary.wiley.com/doi/abs/10.1002/2015GL066170> doi: <https://doi.org/10.1002/2015GL066170>
- Lewkow, N. R., & Kharchenko, V. (2014, August). Precipitation of Energetic Neutral Atoms and Induced Non-thermal Escape Fluxes from the Martian Atmosphere. *ApJ*, *790*(2), 98. doi: 10.1088/0004-637X/790/2/98
- Lillis, R. J., Deighan, J., Fox, J. L., Bougher, S. W., Lee, Y., Combi, M. R., ... Chaufray, J. (2017, March). Photochemical escape of oxygen from Mars: First results from MAVEN in situ data. *J. Geophys. Res. Space Physics*, *122*(3), 3815-3836. doi: 10.1002/2016JA023525
- Mahaffy, P. R., Benna, M., King, T., Harpold, D. N., Arvey, R., Barciniak, M., ... Nolan, J. T. (2015, December). The Neutral Gas and Ion Mass Spectrometer on the Mars Atmosphere and Volatile Evolution Mission. *Space Sci. Rev.*, *195*(1-4), 49-73. doi: 10.1007/s11214-014-0091-1
- Manion, J. A., Huie, R. E., Levin, R. D., Burgess Jr., D. R., Orkin, V. L., Tsang, W., ... Frizzell, D. H. (2015). *NIST Chemical Kinetics Database*. Retrieved 2015-09, from <http://kinetics.nist.gov/>
- Matta, M., Withers, P., & Mendillo, M. (2013, May). The composition of Mars' top-side ionosphere: Effects of hydrogen. *Journal of Geophysical Research (Space Physics)*, *118*(5), 2681-2693. doi: 10.1002/jgra.50104
- Mayyasi, M., Bhattacharyya, D., Clarke, J., Catalano, A., Benna, M., Mahaffy, P., ... Jakosky, B. (2018, September). Significant Space Weather Impact on the Escape of Hydrogen From Mars. *Geophysical Research Letters*, *45*(17), 8844-8852. doi: 10.1029/2018GL077727
- Mayyasi, M., Clarke, J., Bhattacharyya, D., Chaufray, J. Y., Benna, M., Mahaffy, P., ... Jakosky, B. (2019, March). Seasonal Variability of Deuterium in the Upper Atmosphere of Mars. *Journal of Geophysical Research (Space Physics)*, *124*(3), 2152-2164. doi: 10.1029/2018JA026244
- McElroy, D., Walsh, C., Markwick, A. J., Cordiner, M. A., Smith, K., & Millar, T. J. (2013, February). The UMIST database for astrochemistry 2012. *A&A*, *550*, A36. doi: 10.1051/0004-6361/201220465
- Milligan, D. B., & McEwan, M. J. (2000, March). $\text{H}_3^+ + \text{O}$: an experimental study. *Chemical Physics Letters*, *319*(5), 482-485. doi: 10.1016/S0009-2614(00)00154-8
- Millour, E., & Forget, F. (2018). *Mars Climate Database*. Retrieved from <http://www-mars.lmd.jussieu.fr/>
- Mitchell, J. B. A., Novotny, O., LeGarrec, J. L., Florescu-Mitchell, A., Rebrion-Rowe, C., Stolyarov, A. V., ... Andersen, L. H. (2005, May). LETTER TO THE EDITOR: Dissociative recombination of rare gas hydride ions: II. ArH^+ . *Journal of Physics B Atomic Molecular Physics*, *38*(10), L175-L181. doi: 10.1088/0953-4075/38/10/L07
- Molina-Cuberos, G. J., Lichtenegger, H., Schwingenschuh, K., López-Moreno, J. J., & Rodrigo, R. (2002, May). Ion-neutral chemistry model of the lower ionosphere of Mars. *Journal of Geophysical Research (Planets)*, *107*(E5), 5027. doi: 10.1029/2000JE001447
- Nahar, S. N., & Pradhan, A. K. (1997, July). Electron-Ion Recombination Rate Coefficients, Photoionization Cross Sections, and Ionization Fractions for Astrophysically Abundant Elements. I. Carbon and Nitrogen. *ApJS*, *111*(1), 339-355. doi: 10.1086/313013
- Nair, H., Allen, M., Anbar, A. D., & Yung, Y. L. (1994). Photochemical Model of the Martian Atmosphere. *Icarus*, *111*(1), 124-150. doi: 10.1006/icar.1994.1137
- Neary, L., Daerden, F., Aoki, S., Whiteway, J., Clancy, R. T., Smith, M., ... Vandaele, A. C. (2020, April). Explanation for the Increase in High-Altitude Water on Mars Observed by NOMAD During the 2018 Global Dust Storm.

- Geophys. Res. Lett., *47*(7), e84354. doi: 10.1029/2019GL084354
- Nee, J. B., & Lee, L. C. (1984). Photoabsorption cross section of OD at 115-180 nm. *The Journal of Chemical Physics*, *81*(9), 3811–3813. doi: 10.1063/1.448183
- Okabe, H. (1978). *Photochemistry of small molecules*.
- Owen, T., Maillard, J. P., de Bergh, C., & Lutz, B. L. (1988, June). Deuterium on Mars: The Abundance of HDO and the Value of D/H. *Science*, *240*(4860), 1767-1770. doi: 10.1126/science.240.4860.1767
- Praxmarer, C., Hansel, A., & Lindinger, W. (1994, June). Interaction between the ion dipole and the ion-induced dipole in reactions of the polar ion ArH⁺₃. *J. Chem. Phys.*, *100*(12), 8884-8889. doi: 10.1063/1.466691
- Rahmati, A., Larson, D. E., Cravens, T. E., Lillis, R. J., Halekas, J. S., McFadden, J. P., ... Jakosky, B. M. (2018, May). Seasonal Variability of Neutral Escape from Mars as Derived From MAVEN Pickup Ion Observations. *Journal of Geophysical Research (Planets)*, *123*(5), 1192-1202. doi: 10.1029/2018JE005560
- Rosén, S., Derkatch, A., Semaniak, J., Neau, A., Al-Khalili, A., Le Padellec, A., ... Larsson, M. (2000, January). Recombination of simple molecular ions studied in storage ring: dissociative recombination of H₂O⁺. *Faraday Discussions*, *115*, 295-302. doi: 10.1039/a909314a
- Rosén, S., Peverall, R., Larsson, M., Le Padellec, A., Semaniak, J., Larson, Å., ... Dunn, G. H. (1998, June). Absolute cross sections and final-state distributions for dissociative recombination and excitation of CO⁺(v=0) using an ion storage ring. *Phys. Rev. A*, *57*(6), 4462-4471. doi: 10.1103/PhysRevA.57.4462
- Rossi, L., Vals, M., Alday, J., Montmessin, F., Fedorova, A., Trokhimovskiy, A., ... Millour, E. (2022, August). The HDO Cycle on Mars: Comparison of ACS Observations With GCM Simulations. *Journal of Geophysical Research (Planets)*, *127*(8), e07201. doi: 10.1029/2022JE007201
- Sander, S. P., Abbatt, J., Barker, J. R., Burkholder, J. B., Friedl, R. R., Golden, D. M., ... Wine, P. H. (2011). *Chemical Kinetics and Photochemical Data for Use in Atmospheric Studies Evaluation No. 17* (JPL Publication No. 10-6). Pasadena: Jet Propulsion Laboratory. (<http://jpldataeval.jpl.nasa.gov>)
- Scheller, E. L., Ehlmann, B. L., Hu, R., Adams, D. J., & Yung, Y. L. (2021, April). Long-term drying of Mars by sequestration of ocean-scale volumes of water in the crust. *Science*, *372*(6537), 56-62. doi: 10.1126/science.abc7717
- Schunk, R., & Nagy, A. (2009). *Ionospheres: Physics, Plasma Physics, and Chemistry*. doi: 10.1017/CBO9780511635342
- Scott, G. B., Fairley, D. A., Freeman, C. G., McEwan, M. J., Španěl, P., & Smith, D. (1997, March). Gas phase reactions of some positive ions with atomic and molecular hydrogen at 300 K. *J. Chem. Phys.*, *106*(10), 3982-3987. doi: 10.1063/1.473116
- Scott, G. B. I., Fairley, D. A., Freeman, C. G., McEwan, M. J., & Anicich, V. G. (1998, November). Gas-phase reactions of some positive ions with atomic and molecular nitrogen. *J. Chem. Phys.*, *109*(20), 9010-9014. doi: 10.1063/1.477571
- Shematovich, V. I. (2013, November). Suprathermal oxygen and hydrogen atoms in the upper Martian atmosphere. *Solar System Research*, *47*(6), 437-445. doi: 10.1134/S0038094613060087
- Smith, M. A., Schlemmer, S., von Richthofen, J., & Gerlich, D. (2002, October). HOC⁺ + H₂ Isomerization Rate at 25 K: Implications for the Observed [HCO⁺]/[HOC⁺] Ratios in the Interstellar Medium. *ApJ*, *578*(1), L87-L90. doi: 10.1086/344404
- Smith, M. D. (2004). Interannual variability in TES atmospheric observations of Mars during 1999-2003. *Icarus*, *167*(1), 148–165. doi: 10.1016/j.icarus.2003.09.010
- Stone, S. W., Yelle, R. V., Benna, M., Lo, D. Y., Elrod, M. K., & Mahaffy, P. R. (2020, November). Hydrogen escape from Mars is driven by seasonal

- and dust storm transport of water. *Science*, *370*(6518), 824-831. doi: 10.1126/science.aba5229
- Tsang, W., & Hampson, R. F. (1986, July). Chemical Kinetic Data Base for Combustion Chemistry. Part I. Methane and Related Compounds. *Journal of Physical and Chemical Reference Data*, *15*(3), 1087-1279. doi: 10.1063/1.555759
- Tsang, W., & Herron, J. T. (1991, July). Chemical Kinetic Data Base for Propellant Combustion I. Reactions Involving NO, NO₂, HNO, HNO₂, HCN and N₂O. *Journal of Physical and Chemical Reference Data*, *20*(4), 609-663. doi: 10.1063/1.555890
- Tully, J. C. (1975, March). Reactions of O(¹D) with atmospheric molecules. *J. Chem. Phys.*, *62*(5), 1893-1898. doi: 10.1063/1.430675
- Vals, M., Rossi, L., Montmessin, F., Lefèvre, F., Gonzalez-Galindo, F., Fedorova, A., ... Montabone, L. (2022, August). Improved Modeling of Mars' HDO Cycle Using a Mars' Global Climate Model. *Journal of Geophysical Research (Planets)*, *127*(8), e07192. doi: 10.1029/2022JE007192
- Vandaele, A. C., Korablev, O., Daerden, F., Aoki, S., Thomas, I. R., Altieri, F., ... Smith, M. D. e. a. (2019). Martian dust storm impact on atmospheric H₂O and D/H observed by ExoMars Trace Gas Orbiter. *Nature*, *568*(7753), 521-525. doi: 10.1038/s41586-019-1097-3
- Viggiano, A. A., Albritton, D. L., Fehsenfeld, F. C., Adams, N. G., Smith, D., & Howorka, F. (1980, March). Laboratory studies of some ion-atom reactions related to interstellar molecular synthesis. *ApJ*, *236*, 492-497. doi: 10.1086/157766
- Viggiano, A. A., Ehlerding, A., Hellberg, F., Thomas, R. D., Zhaunerchyk, V., Gepfert, W. D., ... Österdahl, F. (2005, June). Rate constants and branching ratios for the dissociative recombination of CO₂⁺. *J. Chem. Phys.*, *122*(22), 226101-226101. doi: 10.1063/1.1926283
- Villanueva, G. L., Liuzzi, G., Aoki, S., Stone, S. W., Brines, A., Thomas, I. R., ... Vandaele, A. C. (2022, June). The Deuterium Isotopic Ratio of Water Released From the Martian Caps as Measured With TGO/NOMAD. *Geophys. Res. Lett.*, *49*(12), e98161. doi: 10.1029/2022GL098161
- Villanueva, G. L., Liuzzi, G., Crismani, M. M. J., Aoki, S., Vandaele, A. C., Daerden, F., ... Lopez-Moreno, J. J. (2021, February). Water heavily fractionated as it ascends on Mars as revealed by ExoMars/NOMAD. *Science Advances*, *7*(7), eabc8843. doi: 10.1126/sciadv.abc8843
- Villanueva, G. L., Mumma, M. J., Novak, R. E., Käuff, H. U., Hartogh, P., Encrenaz, T., ... Smith, M. D. (2015, April). Strong water isotopic anomalies in the martian atmosphere: Probing current and ancient reservoirs. *Science*, *348*(6231), 218-221. doi: 10.1126/science.aaa3630
- Vuitton, V., Yelle, R. V., Klippenstein, S. J., Hörst, S. M., & Lavvas, P. (2019). Simulating the density of organic species in the atmosphere of Titan with a coupled ion-neutral photochemical model. *Icarus*, *324*, 120-197. (Publisher: Elsevier Inc.) doi: 10.1016/j.icarus.2018.06.013
- Wakelam, V., & Gratier, P. (2019). *Kinetic Database for Astrochemistry*. Retrieved from <http://kida.obs.u-bordeaux1.fr/contact.html>
- Wernicke, L. J., & Jakosky, B. M. (2021, March). Martian Hydrated Minerals: A Significant Water Sink. *Journal of Geophysical Research (Planets)*, *126*(3), e06351. doi: 10.1029/2019JE006351
- Woods, T. N., Chamberlin, P. C., Harder, J. W., Hock, R. A., Snow, M., Eparvier, F. G., ... Richard, E. C. (2019). *LISIRD (LASP Interactive Solar Irradiance Datacenter)*. Retrieved from <http://lasp.colorado.edu/lisird/>
- Wordsworth, R. (2016). The Climate of Early Mars. *Annual Review of Earth and Planetary Sciences*, *44*, 381-408. doi: 10.1146/annurev-earth-060115-012355
- Yoshida, T., & Kuramoto, K. (2020, July). Sluggish hydrodynamic escape of early Martian atmosphere with reduced chemical compositions. *Icarus*, *345*, 113740.

doi: 10.1016/j.icarus.2020.113740

- Yu, H.-G., Muckerman, J. T., & Francisco, J. S. (2005). Direct ab initio dynamics study of the $\text{OH} + \text{HCO}$ reaction. *The Journal of Physical Chemistry A*, *109*(23), 5230–5236.
- Yung, Y. L., & DeMore, W. B. (1998). *Photochemistry of Planetary Atmospheres*. Oxford University Press.
- Yung, Y. L., Wen, J.-S., Moses, J. I., Landry, B. M., Allen, M., & Hsu, K.-J. (1989, October). Hydrogen and deuterium loss from the terrestrial atmosphere: A quantitative assessment of nonthermal escape fluxes. *J. Geophys. Res.*, *94*(D12), 14971–14989. doi: 10.1029/JD094iD12p14971
- Yung, Y. L., Wen, J.-S., Pinto, J. P., Allen, M., Pierce, K. K., & Paulson, S. (1988, October). HDO in the Martian atmosphere: Implications for the abundance of crustal water. *Icarus*, *76*(1), 146–159. doi: 10.1016/0019-1035(88)90147-9
- Zahnle, K., Haberle, R. M., Catling, D. C., & Kasting, J. F. (n.d.). Photochemical instability of the ancient Martian atmosphere. *Journal of Geophysical Research E: Planets*, *113*(E11), 1–16.
- Zahnle, K., Kasting, J. F., & Pollack, J. B. (1990, April). Mass fractionation of noble gases in diffusion-limited hydrodynamic hydrogen escape. *Icarus*, *84*(2), 502–527. doi: 10.1016/0019-1035(90)90050-J
- Zanchet, A., Bussery-Honvault, B., Jorfi, M., & Honvault, P. (2009, January). Study of the $\text{C}(3\text{P}) + \text{OH}(X2\Pi) \rightarrow \text{CO}(a3\Pi) + \text{H}(2\text{S})$ reaction: fully global ab initio potential energy surfaces of the $12\text{A}''$ and $14\text{A}''$ excited states and non adiabatic couplings. *Physical Chemistry Chemical Physics (Incorporating Faraday Transactions)*, *11*(29), 6182. doi: 10.1039/b903829a
- Zhang, P., Kharchenko, V., Jamieson, M. J., & Dalgarno, A. (2009, July). Energy relaxation in collisions of hydrogen and deuterium with oxygen atoms: OH AND OD COLLISION ENERGY RELAXATION. *J. Geophys. Res.*, *114*(A7), 1–14. Retrieved from <http://doi.wiley.com/10.1029/2009JA014055> doi: 10.1029/2009JA014055
- Španěl, P., Dittrichová, L., & Smith, D. (1993, November). FALP studies of the dissociative recombination coefficients for O_2^+ and NO^+ within the electron temperature range 300–2000 K. *International Journal of Mass Spectrometry and Ion Processes*, *129*, 183–191. doi: 10.1016/0168-1176(93)87041-P